Targeting Observations Using Singular Vectors

R. BUIZZA

European Centre for Medium-Range Weather Forecasts, Reading, Berkshire, United Kingdom

A. MONTANI

Department of Meteorology, University of Reading, Reading, Berkshire, United Kingdom

(Manuscript received 20 April 1998, in final form 9 December 1998)

ABSTRACT

Singular vectors with maximum energy at final time inside a *verification area* are used to identify the *target area* where extra observations should be taken, at an initial time, to reduce the forecast error inside the verification area itself. This technique is applied to five cases of cyclone development in the Atlantic Ocean, with cyclones reaching the British Isles at the final time. Three verification areas centered around this region are considered.

First, the sensitivity of the target area to the choice of the forecast trajectory along which the singular vectors are evolved, to the choice of the verification area where singular vector energy is maximized, and to the number of singular vectors used to define the target area is investigated. Results show little sensitivity to the choice of the verification area, but high sensitivity to the choice of the trajectory. Regarding the number of singular vectors used, results based on the first 4 or the first 10 singular vectors are shown to be very similar.

Second, the potential forecast error reduction that could be achieved by taking extra observations inside the target area is estimated by contrasting the error of a forecast started from the unperturbed analysis with the error of a forecast started by subtracting so-called pseudo-inverse perturbations (estimated using the leading singular vectors) to the unperturbed analysis. Results indicate that root-mean-square errors in the verification region could be reduced by up to 13% by adding targeted observations.

Overall, results suggest that linear models can be used to define the target area where adaptive observations should be taken.

1. Introduction

The dominant singular vectors of the integral linear propagator for a nonlinear dynamical system provide information about maximum perturbation growth (measured by a given norm) during finite time intervals, and can be used to estimate the evolution of initial errors during the course of a forecast (Lacarra and Talagrand 1988; Farrell 1990; Borges and Hartmann 1992). Singular vectors are currently used at the European Centre for Medium-Range Weather Forecasts (ECMWF) in the construction of the initial perturbations of the Ensemble Prediction System (Buizza and Palmer 1995; Molteni et al. 1996).

Consider a meteorological system evolving between time t_0 and t, localized at final time t inside a geographical area Σ_t (hereafter verification area). Suppose that extra observations could be taken inside a geographical area Σ_0 at initial time t_0 (hereafter target area), with the purpose of improving the time t forecast inside Σ_t.

This work aims to achieve two goals. First, it wants to prove that few singular vectors optimized to maximize growth inside the verification region Σ_t can be used to define the target area Σ_0. The rationale for the use of the singular vectors is that the most important source of forecast error is related to analysis error components projecting onto growing phase space directions, and that the singular vectors project onto these directions. This follows experiments that demonstrated that forecast error can be reduced by perturbing the initial conditions using perturbations generated using singular vectors (Buizza et al. 1997). Second, it wants to estimate the potential forecast error reduction that could be achieved by taking adaptive observations in the target area Σ_0. This second goal is achieved by comparing forecasts starting from the analysis with forecasts started from the analysis perturbed using so-called pseudo-inverse initial perturbations generated using the leading singular vectors.

Following the results described in this work, which were briefly documented in Montani et al. (1996), ECMWF singular vectors have been used in real-time application for targeting observation during the Fronts and Atlantic Storm Track Experiment (FASTEX; Joly

Corresponding author address: Dr. Roberto Buizza, ECMWF, Shinfield Park, Reading, Berkshire RG2 9AX, United Kingdom.
E-mail: r.buizza@ecmwf.int

et al. 1996, Snyder 1996). Other strategies were used during FASTEX to target adaptive observations. Langland and Rohaly (1996), following the work of Rabier et al. (1996) on sensitivity vectors, used the lower-tropospheric vorticity of the forecast state as cost function and proposed that observations should be targeted in the region where the sensitivity field is maximum. This proposal is closely related to the singular vector technique proposed in this paper, both being adjoint-based methods [on this aspect see also Gelaro et al. (1998)]. Note that a similar technique, based on the use of a quasi-inverse linear model, was also proposed by Pu et al. (1997, 1998).

Bishop and Toth (1998) introduced the ensemble transform technique, in which linear combinations of ensemble perturbations are used to estimate the prediction error variance associated with different possible deployments of observational resources. The deployment of observational resources that minimizes the ensemble transform estimate of prediction error variance is deemed optimal. This technique was applied during FASTEX to the National Centers for Environmental Prediction (Toth and Kalnay 1993, 1996), the Canadian (Houtekamer et al. 1996), and the ECMWF ensemble systems.

A more subjective strategy was also used during FASTEX to target observations. Following Hoskins et al. (1985) and Appenzeller et al. (1996), this strategy was based on the use of potential vorticity to analyze atmospheric developments.

This paper concentrates only on the singular vector technique and addresses a number of sensitivity issues related to the proposed technique [the reader is referred to Palmer et al. (1998) for a brief discussion on the similarities and differences among the strategies]. Five cases of cyclone developments in the Atlantic Ocean during January, February, and March 1996 are discussed. The sensitivity of the proposed technique to the definition of the trajectory along which singular vectors are evolved, to the choice of the verification area, and to the number of singular vectors used to define the target area is investigated. Two issues of great interest for the planning of real-time targeting experiments, the accuracy of the linear approximation (onto which adjoint methods are based), and the potential forecast error reduction that real-time targeting could achieve, are also discussed in this work.

The methodology of targeting observations using singular vectors is presented in section 2, and the experimental setup is described in section 3. The synoptic description of the five case studies is reported in section 4. Issues related to the proposed technique and sensitivity analyses are discussed in section 5. The problem of estimating the possible forecast error reduction is investigated in section 6. Further sensitivity results are discussed in section 7. Conclusions are drawn in section 8.

2. Methodology

The reader is referred to Buizza and Palmer (1995) for a thorough description of the singular vector approach to atmospheric predictability.

a. Targeted singular vectors

Let $\mathbf{x}$ be the state vector of the atmosphere, whose evolution equations can be written in a symbolic way as

$$\frac{\partial \mathbf{x}}{\partial t} = \mathbf{A}(\mathbf{x}). \tag{1}$$

Denote by $\mathbf{x}(t)$ a nonlinear integration of Eq. (1). The time evolution of small perturbations $\boldsymbol{\delta}\mathbf{x}$ around the time-evolving trajectory $\mathbf{x}(t)$ can be described, in a first approximation, by the linearized model equations

$$\frac{\partial \boldsymbol{\delta}\mathbf{x}}{\partial t} = \mathbf{A}_l \boldsymbol{\delta}\mathbf{x}, \tag{2}$$

where $\mathbf{A}_t \equiv \partial \mathbf{A}(\mathbf{x})/\partial \mathbf{x}|_{\mathbf{x}(t)}$ is the tangent operator computed at the trajectory point $\mathbf{x}(t)$.

Let $\mathbf{L}(t, t_0) + \mathbf{L}'(t, t_0)$ be the integral forward propagator of the dynamical equations [(2)] linearized about a nonlinear trajectory $\mathbf{x}(t)$,

$$\boldsymbol{\delta}\mathbf{x}(t) = [\mathbf{L}(t, t_0) + \mathbf{L}'(t, t_0)]\boldsymbol{\delta}\mathbf{x}(t_0), \tag{3}$$

that maps a perturbation $\boldsymbol{\delta}\mathbf{x}$ at initial time t_0 to optimization time t, where $\mathbf{L}(t, t_0)$ represents the components of the tangent forward propagator that, at the time of this work, were included in the linear version (these include the adiabatic processes, horizontal diffusion, vertical diffusion, and surface drag; Buizza 1994a), and $\mathbf{L}'(t, t_0)$ represents the components of the tangent propagator that were not included in the linear version (these include, e.g., the linearized versions of radiation, convection, and gravity wave drag).

Consider two perturbations, $\boldsymbol{\delta}\mathbf{x}$ and $\boldsymbol{\delta}\mathbf{y}$, and a positive definite Hermitian matrix $\mathbf{E}$, and define an inner product $(\cdot\,;\cdot)_E$ on the tangent phase space,

$$(\boldsymbol{\delta}\mathbf{x};\ \boldsymbol{\delta}\mathbf{y})_E \equiv \langle \boldsymbol{\delta}\mathbf{x};\ \mathbf{E}\boldsymbol{\delta}\mathbf{y}\rangle, \tag{4}$$

where $\langle \cdot\,;\cdot\rangle$ identifies the canonical Euclidean scalar product. Denote by $\|\cdot\|_E$ the norm associated with the inner product $(\cdot\,;\cdot)_E$.

Let $\mathbf{L}^{*E}$ be the adjoint of the linear version $\mathbf{L}$ with respect to the inner product $(\cdot\,;\cdot)_E$,

$$(\mathbf{L}^{*E}\boldsymbol{\delta}\mathbf{x};\ \boldsymbol{\delta}\mathbf{y})_E = (\boldsymbol{\delta}\mathbf{x};\ \mathbf{L}\boldsymbol{\delta}\mathbf{y})_E. \tag{5}$$

The squared norm of a perturbation $\boldsymbol{\delta}\mathbf{x}$ at time t is given by

$$\|\boldsymbol{\delta}\mathbf{x}(t)\|_E^2 = (\boldsymbol{\delta}\mathbf{x}(t_0);\ \mathbf{L}^{*E}\mathbf{L}\boldsymbol{\delta}\mathbf{x}(t_0))_E. \tag{6}$$

The phase space directions $\boldsymbol{\delta}\mathbf{x}$ for which $\|\boldsymbol{\delta}\mathbf{x}(t)\|_E/\|\boldsymbol{\delta}\mathbf{x}(t_0)\|_E$ is maximum are the eigenvectors $\mathbf{v}_i(t_0)$,

$$\mathbf{L}^{*E}\mathbf{L}\mathbf{v}_i(t_0) = \sigma_i^2\mathbf{v}_i(t_0), \tag{7}$$

TABLE 1. Final time verification areas for all case studies.

Case study	Final time verification area Σ_t		
	Area A	Area B	Area C
96.01.02 → 04	(−20°: 0°; 40°–60°)	(−15°: 5°; 40°–60°)	(−30°: 10°; 30°–70°)
96.01.06 → 08	(−20°: 0°; 40°–60°)	(−25°: −5°; 40°–40°)	(−30°: 10°; 30°–70°)
96.02.05 → 07	(−20°: 0°; 40°–60°)	(−15°: 5°; 40°–60°)	(−30°: 10°; 30°–70°)
96.02.07 → 09	(−20°: 0°; 40°–60°)	(−20°: 0°; 45°–65°)	(−30°: 10°; 30°–70°)
96.03.10 → 12	(−20°: 0°; 40°–60°)	(−20°: 0°; 50°–70°)	(−30°: 10°; 30°–70°)

with largest eigenvalues σ_i^2.

The square roots of the eigenvalues, σ_i, are called the *singular values* and the eigenvectors $\mathbf{v}_i(t_0)$ the (right) singular vectors of $\mathbf{L}$ with respect to the inner product $\mathbf{E}$ (see, e.g., Noble and Daniel 1977). The singular vectors with largest singular values identify the directions characterized by maximum growth. The time interval $t - t_0$ is called the optimization time interval.

Denote by $\boldsymbol{\delta x}_g(t)$ the gridpoint representation of the state vector $\boldsymbol{\delta x}(t)$; by $\mathbf{S}$ the spectral-to-gridpoint transformation operator $\boldsymbol{\delta x}_g = \mathbf{S}\boldsymbol{\delta x}$; and by $\mathbf{G}\boldsymbol{\delta x}_g$ the multiplication of the vector $\boldsymbol{\delta x}_g$ by the gridpoint function $g(s)$:

$$g(s) = 1 \text{ if } s \in \Sigma_t \qquad g(s) = 0 \text{ if } s \notin \Sigma_t, \quad (8)$$

where s defines the coordinate of a grid point, and Σ_t is the verification area.

The application of the local projection operator $\mathbf{T} \equiv \mathbf{S}^{-1}\mathbf{G}\mathbf{S}$ to the vector $\boldsymbol{\delta x}(t)$ sets the vector $\boldsymbol{\delta x}(t)$ to have zero gridpoint values outside the geographical region Σ_t (Buizza 1994b). The local projection operator $\mathbf{T}$ can be used to compute singular vectors with maximum final time norm inside the verification area Σ_t, by searching for the eigenvectors of the operator

$$\mathbf{K} = \mathbf{E}^{-1/2}\mathbf{L}^{*E}\mathbf{T}\mathbf{L}\mathbf{E}^{-1/2}. \quad (9)$$

b. Target area definition

The initial time structure of the singular vectors with largest $\mathbf{E}$ norm inside the verification region Σ_t can be used to identify the *target area* Σ_0. Since the singular vectors have been constructed to maximize the ratio of the $\mathbf{E}$ norm at final and initial times, it is proposed to use the $\mathbf{E}$ norm of the singular vectors at initial time to identify Σ_0.

Consider the first M singular vectors at initial time $\mathbf{v}_i(t_0)$ with unit $\mathbf{E}$ norm, and denote by $f_i^E(\lambda, \phi, p)$ the value of the $\mathbf{E}$ norm of the ith singular vector at the grid point (λ, ϕ, p), where λ denotes longitude, ϕ denotes latitude, and p denotes a vertical coordinate [in case of $\mathbf{E}$ being total energy; e.g., $f_i^E(\lambda, \phi, p)$ would be the sum of the grid point value of the kinetic and potential energy]. Denote by $F_M^E(\lambda, \phi, p)$ the weighted sum

$$F_M^E(\lambda, \phi, p) \equiv \sum_{i=1}^{M} \left(\frac{\sigma_i}{\sigma_1}\right) f_i^E(\lambda, \phi, p), \quad (10)$$

and denote by s_0 the location where the function F_M^E is maximum,

TABLE 2. Schematic of the different types of trajectory used for the singular vector computations with verification time 1200 UTC 12 March.

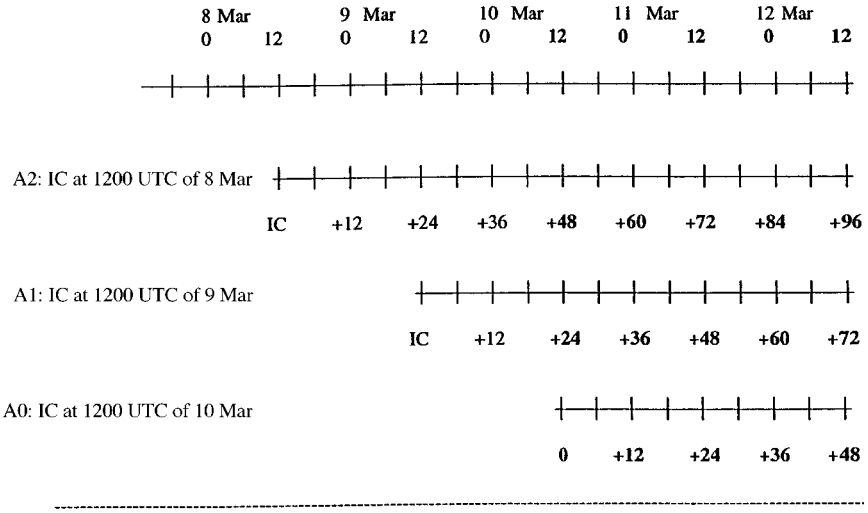

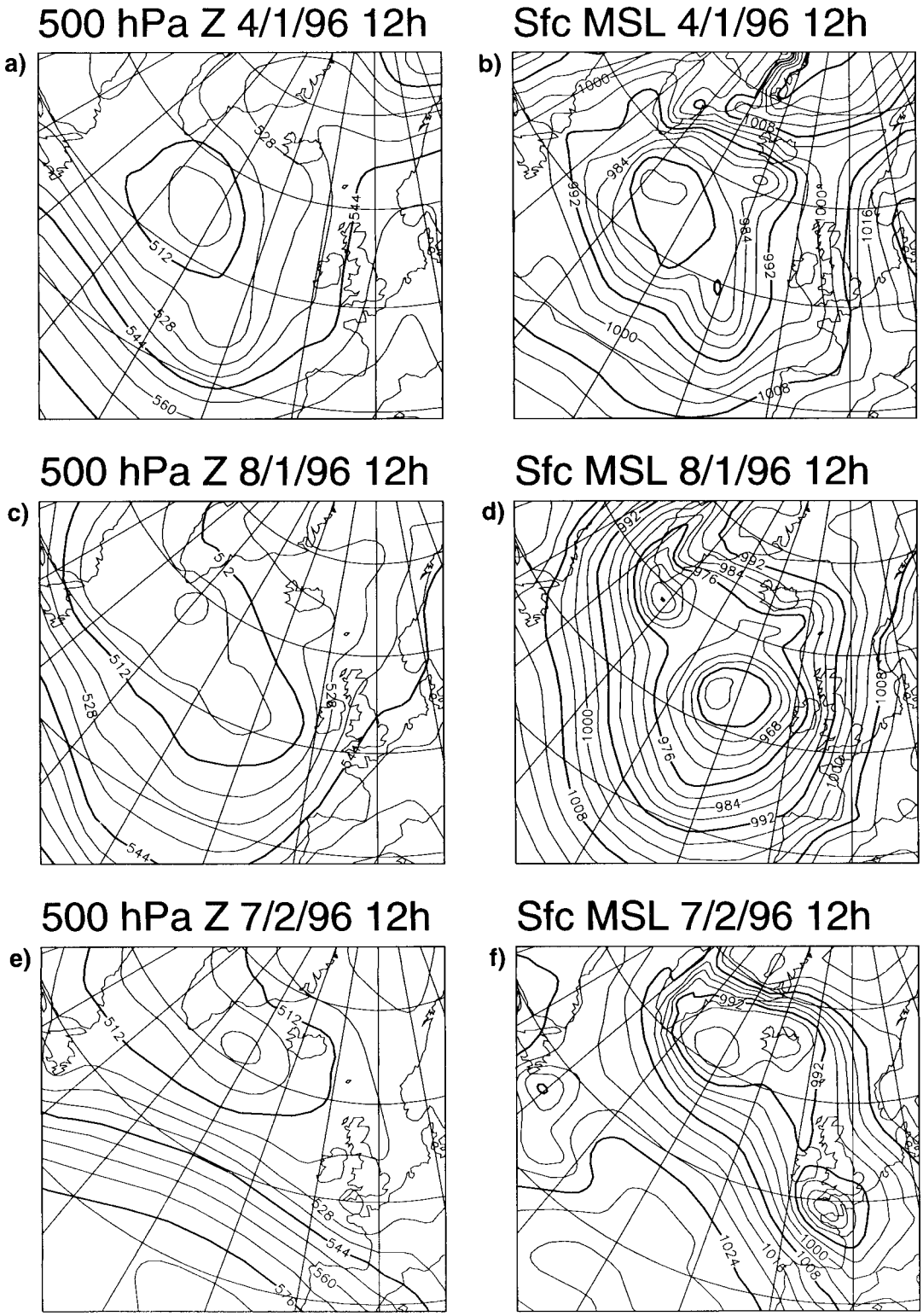

FIG. 1. The 500-hPa geopotential height at 1200 UTC for (a) 4 Jan, (c) 8 Jan, (e) 7 Feb, (g) 9 Feb, and (i) 12 Mar 1996; and mean sea level pressure at 1200 UTC for (b) 4 Jan, (d) 8 Jan, (f) 7 Feb, (h) 9 Feb, and (j) 12 Mar 1996. Contour interval is 8 dam for geopotential and 4 mb for mean sea level pressure.

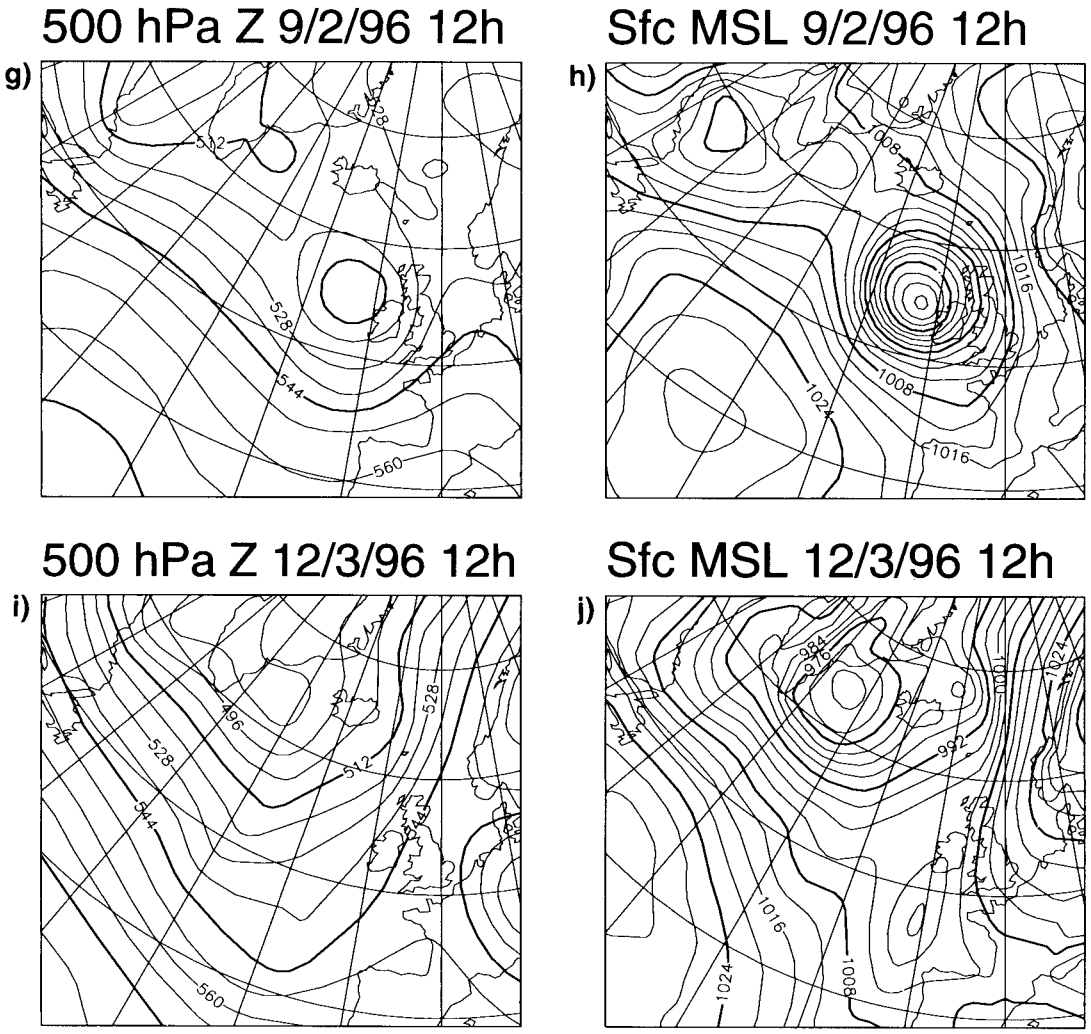

FIG. 1. (*Continued*)

$$F_M^E(s_0) \geq F_M^E(s) \quad \forall s. \tag{11}$$

The target area Σ_0 is defined by the grid points where the function F_M^E is larger than a certain value, specifically 0.5 times its maximum:

$$s \in \Sigma_0 \quad \text{if} \quad F_M^E(s) \geq 0.5 F_M^E(s_0). \tag{12}$$

Note that, in Eq. (10), the weights (σ_i/σ_1) have been introduced to consider that singular vectors with different ranking order grow with different amplification factors, the first one growing fastest. In fact, given two perturbations with the same norm and, for example, parallel in phase space to singular vectors numbers 1 and 4, the perturbation located in the region where the first singular vector is localized grows more than that localized in the region where the singular vector number 4 is localized. If these perturbations identify analysis errors, then the first one will deteriorate the forecast accuracy more than the second one. Thus, since it is more important to reduce the analysis error in the first rather than in the second region, more weight should be given to the first rather than the second region.

c. Forecast error projection onto singular vectors

As in Buizza et al. (1997), denote by $\mathbf{u}_i(t)$ a set of normalized vectors constructed using the final time singular vectors,

$$\mathbf{u}_i \equiv \frac{\mathbf{v}_i(t)}{\sigma_i}; \tag{13}$$

denote by $\mathbf{V} = [\mathbf{v}_1(t_0), \ldots, \mathbf{v}_M(t_0)]$ the $N \times M$ matrix with columns $\mathbf{v}_i(t_0)$, by $\mathbf{U} = [\mathbf{u}_1, \ldots, \mathbf{u}_M]$ the $N \times M$ matrix with columns $\mathbf{u}_i$; and denote by $\mathbf{D}$ the $M \times M$ diagonal matrix with elements σ_i. Equation (13) can be written as

$$\mathbf{UD} = \mathbf{LV}. \tag{14}$$

From Eq. (14), it follows that the tangent forward propagator $\mathbf{L}$ in the unstable subspace is given by

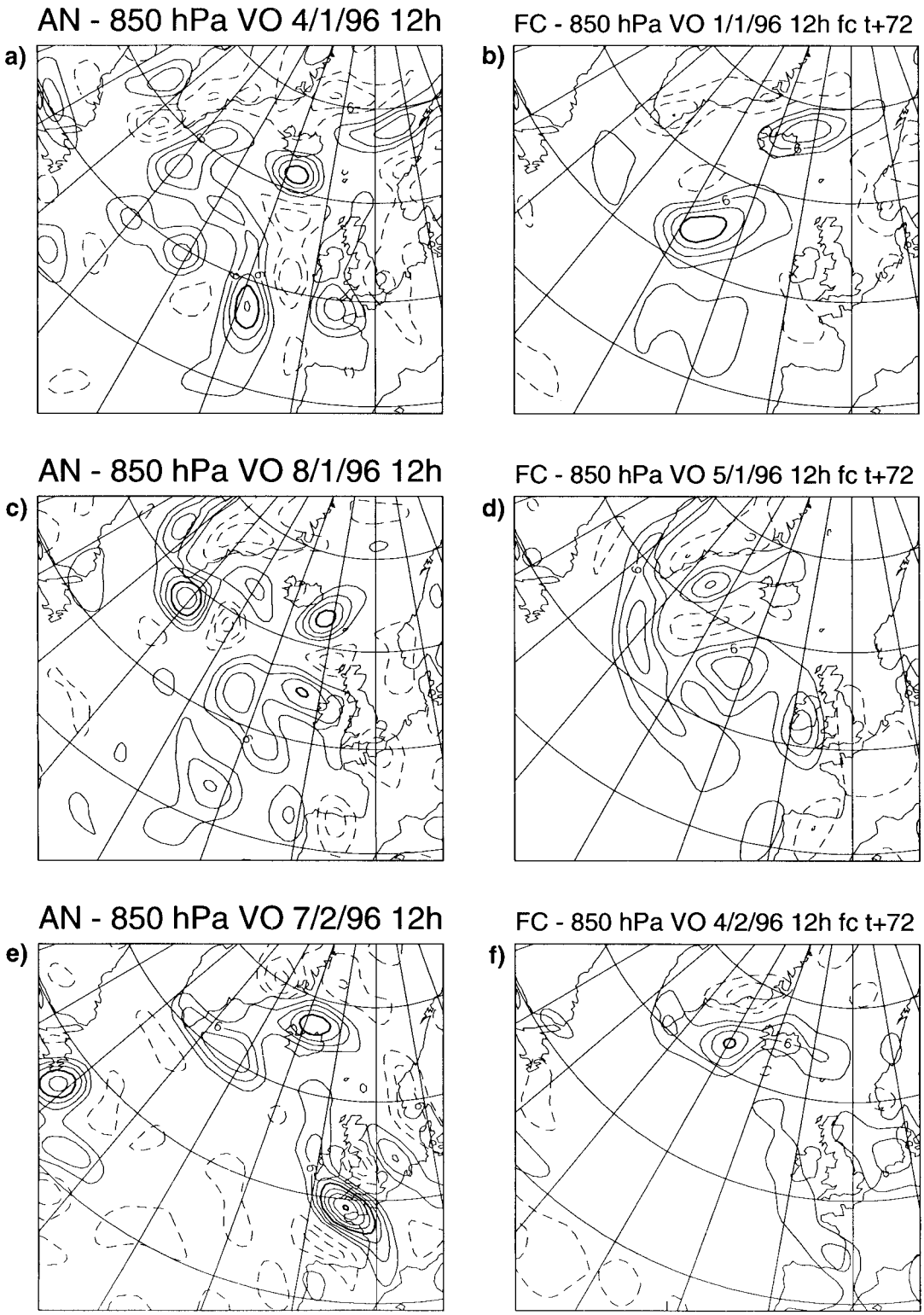

FIG. 2. The 850-hPa vorticity analysis at 1200 UTC for (a) 4 Jan, (c) 8 Jan, (e) 7 Feb, (g) 9 Feb, and (i) 12 Mar 1996; and the 72-h forecast verifying at 1200 UTC for (b) 4 Jan, (d) 8 Jan, (f) 7 Feb, (h) 9 Feb, and (j) 12 Mar 1996. Contour interval is 3×10^{-5} s^{-1}.

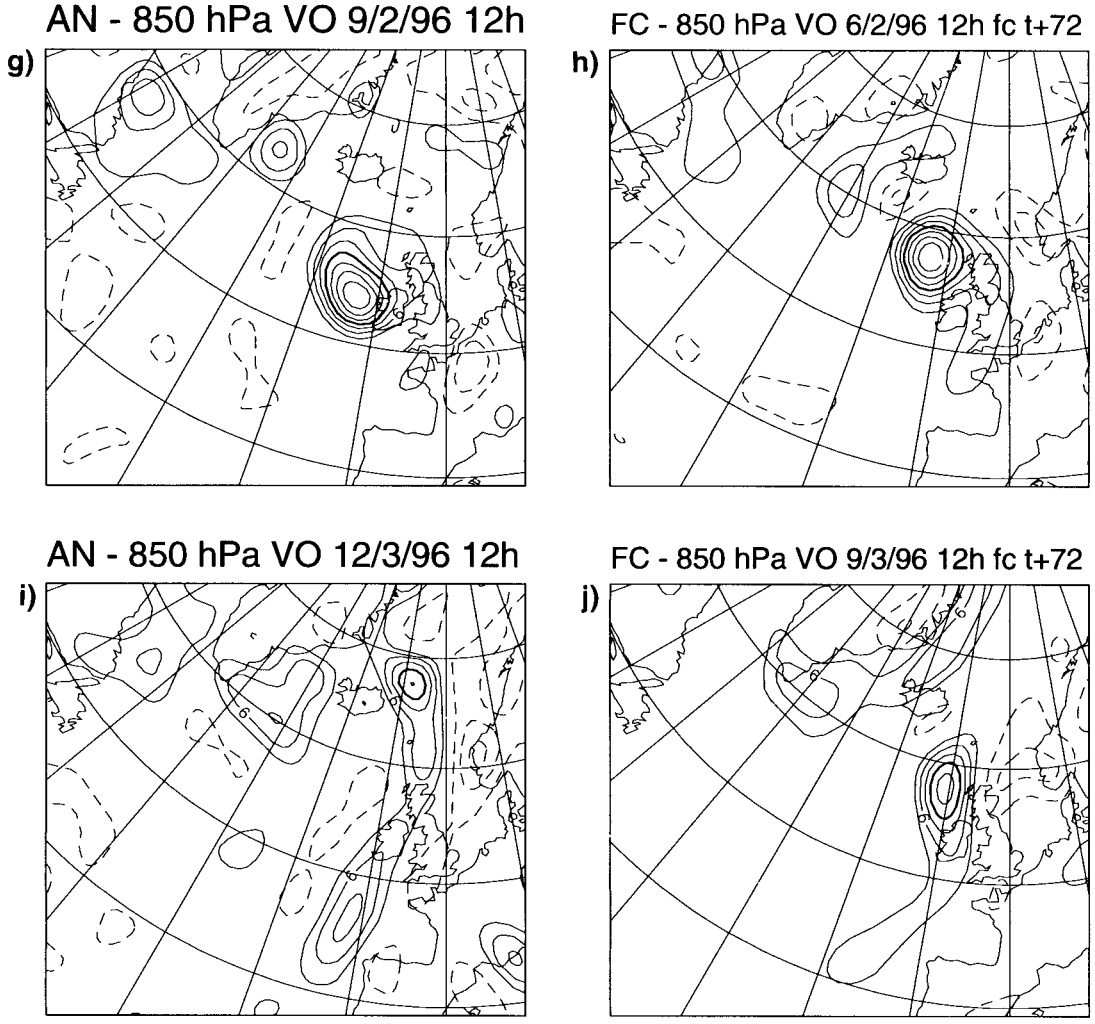

FIG. 2. (*Continued*)

$$\tilde{\mathbf{L}} \equiv \mathbf{U}\mathbf{D}\mathbf{V}^{\mathrm{T}}. \tag{15}$$

Consider a vector $\boldsymbol{\delta}\mathbf{e}(t)$ representing the error of the time t forecast $\mathbf{c}(t)$ (''control'' forecast) started from the unperturbed analysis $\mathbf{a}(t_0)$, that is, $\boldsymbol{\delta}\mathbf{e}(t) = \mathbf{c}(t) - \mathbf{a}(t)$. The projection of $\boldsymbol{\delta}\mathbf{e}(t)$ onto the unstable subspace spanned by the vectors $\mathbf{u}_i(t)$ is given by

$$\boldsymbol{\delta}\tilde{\mathbf{e}}(t) = \sum_{i=1}^{M} \mathbf{u}_i(\mathbf{u}_i;\ \boldsymbol{\delta}\mathbf{e}(t))_E. \tag{16}$$

To calculate the initial time vector $\boldsymbol{\delta}\tilde{\mathbf{e}}(t_0)$, which evolves to $\boldsymbol{\delta}\tilde{\mathbf{e}}(t)$, from Eq. (15), it follows that an estimate of the inverse of the tangent forward propagator is given by

$$\tilde{\mathbf{L}}^{-1} \equiv \mathbf{V}\mathbf{D}^{-1}\mathbf{U}^{\mathrm{T}}, \tag{17}$$

and thus

$$\boldsymbol{\delta}\tilde{\mathbf{e}}(t_0) \equiv \tilde{\mathbf{L}}^{-1}\boldsymbol{\delta}\mathbf{e}(t) = \mathbf{V}\mathbf{D}^{-1}\mathbf{U}^{\mathrm{T}}\boldsymbol{\delta}\mathbf{e}(t). \tag{18}$$

Equation (18) is the analog, in the unstable subspace, of inverting the forward propagator $\mathbf{L}$ to obtain the initial state. The vector $\boldsymbol{\delta}\tilde{\mathbf{e}}(t_0)$, which can be considered an estimate of the growing component of the analysis error, is called pseudo-inverse initial perturbation (Buizza et al. 1997; Gelaro et al. 1998). As indicated by Eq. (18), the pseudo-inverse initial perturbation is a linear combination of the singular vectors at initial time, with coefficients computed by projecting the forecast error onto the evolved singular vectors.

d. Potential forecast error reduction

Extra observations taken in the target area Σ_0 are used to define the increment $\boldsymbol{\delta}\mathbf{a}_0$ to be added to the unperturbed analysis $\mathbf{a}(t_0)$ to reduce the forecast error. If the time evolution of the increment $\boldsymbol{\delta}\mathbf{a}_0$ can be described to a good degree by the estimated linear propagator $\tilde{\mathbf{L}}$, then Eq. (18) says that a good estimate of $\boldsymbol{\delta}\mathbf{a}_0$ is given by $-\boldsymbol{\delta}\tilde{\mathbf{e}}(t_0)$. In other words, considering two nonlinear integrations, one started from the analysis $\mathbf{a}(t_0)$ and one

TABLE 3a. Mean and the standard deviation of the similarity indexes computed between the first 10 singular vectors evolving along different types of trajectories at initial time, but with the same verification area.

Trajectory	0 vs 1		0 vs 2		1 vs 2	
	s_m	s_{std}	s_m	s_{std}	s_m	s_{std}
Area A	59	8	38	8	45	11
Area B	60	7	35	8	43	11
Area C	62	9	37	6	45	11

TABLE 3b. As in Table 3a but for singular vectors evolving along the same trajectory but with different verification area.

Verification area	A vs B		A vs C		B vs C	
	s_m	s_{std}	s_m	s_{std}	s_m	s_{std}
Trajectory 0	77	12	75	2	66	9
Trajectory 1	79	11	78	11	71	8
Trajectory 2	81	14	73	8	69	10

started from the perturbed analysis $\mathbf{a}(t_0) - \boldsymbol{\delta}\tilde{\mathbf{e}}(t_0)$, the difference between the error of the two forecasts measures the capability of the first M targeted singular vectors to capture the growing features of analysis error. Moreover, this difference can be used to estimate the possible forecast error reduction that could be achieved by adding extra observation in the target area Σ_0. A similar approach was used by Bishop and Toth (1998).

3. Experimental setup

Singular vectors depend on resolution, on the optimization time interval, on the verification area Σ_t, on the norm $\mathbf{E}$, and on the forecast trajectory along which the model is linearized. Furthermore, the target area Σ_0 defined in Eq. (12) and the pseudo-inverse initial perturbation $\boldsymbol{\delta}\tilde{\mathbf{e}}(t_0)$ computed in Eq. (18) depend also on the number of singular vectors used to compute the gridpoint function F_M^E and to estimate the inverse of the tangent forward propagator. Experiments have been set up as follows.

a. Singular vector definition

Singular vectors have been computed at spectral triangular truncation T63 and with 19 vertical levels (T63L19). A T63L19 is used instead of the operational T42L31 to have finer resolution for a more accurate targeting. The reader is referred to Buizza (1998) for sensitivity studies on the impact of horizontal resolution on singular vectors. Concerning vertical resolution, experiments have indicated that there are few differences between using 19 or 31 vertical levels (not shown).

A 48-h optimization time interval has been used throughout this paper. A longer forecast time has not been used because results suggested that, for perturbations defined by singular vectors and characterized by an initial amplitude comparable to analysis error estimates, the time evolution can be linearly approximated only up to 48 h.

Palmer et al. (1998) showed that singular vectors depend strongly on the norm definition. Since the purpose of targeting observations is to reduce the forecast error, the best choice for a metric would be one based on the second moment of the analysis error probability distribution. An estimate of such a metric is possible from variational data assimilation schemes (Courtier et al. 1993), and the work of Barkmeijer et al. (1998) has proved that, using a low-resolution T21L5 primitive equation model, singular vectors can be computed using such a metric [the reader is referred to Palmer et al. (1998) and Barkmeijer et al. (1998) for more discussion on these issues]. One of the conclusions of Palmer et al. (1998) was that total energy is a reasonable first-order estimate of such a metric [this conclusion supported earlier results by Molteni et al. (1996)]. Following this conclusion, and since singular vector computation at T63L19 resolution using a metric based on the second moment of the analysis error probability distribution requires too many computer resources, the total energy norm has been used both at initial and final time.

Up to 10 singular vectors have been computed (computer resources availability did not allow the computation of more than 10 singular vectors at T63L19 resolution). Results obtained using only the leading singular vector, the first four singular vectors, or all the first 10 singular vectors will be compared.

Since this work focuses on the analysis of cyclonic developments in the Atlantic Ocean arriving at verification time close to the British Isles, only verification areas centered around this region have been considered. More specifically, for each case study three different verification areas have been used, two fixed and one case dependent, centered at the location (inside the British Isles region) where the analyzed vorticity at 850 hPa had a maximum value. The fact that the case-dependent verification areas have been defined using information from the analysis field should be stressed. Table 1 lists, for each case study, the coordinates of the three areas. Note that areas A and B have a $20^\circ \times 20^\circ$ size, while area C has a $40^\circ \times 40^\circ$ size.

b. Trajectory definition

Suppose that extra observations are to be made at 1200 UTC 10 March 1996 to improve the 48-h forecast. Suppose that observations are going to be taken by dropsondes released by an aircraft, and that the flight crew needs to be alerted at least nine hours in advance (i.e., 0300 UTC 10 March), so to have time to prepare the flight plan, to fly into the target area and to release the sondes exactly at the target time (personal experience during field experiments has indicated that at least nine hours are needed; C. Bishop 1998, personal communication).

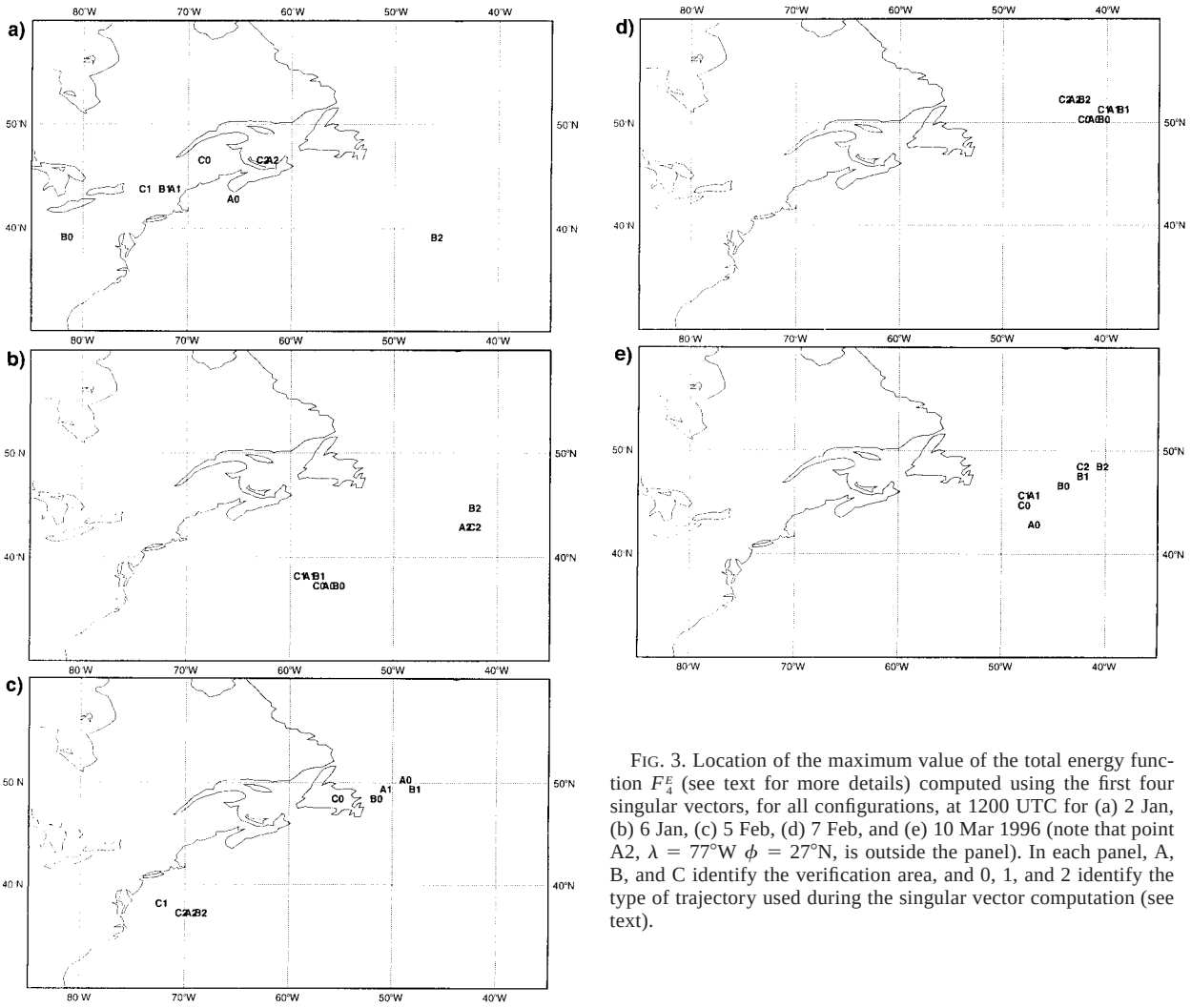

FIG. 3. Location of the maximum value of the total energy function F_4^E (see text for more details) computed using the first four singular vectors, for all configurations, at 1200 UTC for (a) 2 Jan, (b) 6 Jan, (c) 5 Feb, (d) 7 Feb, and (e) 10 Mar 1996 (note that point A2, $\lambda = 77°\text{W}$ $\phi = 27°\text{N}$, is outside the panel). In each panel, A, B, and C identify the verification area, and 0, 1, and 2 identify the type of trajectory used during the singular vector computation (see text).

At ECMWF, the 24-h forecast started at 1200 UTC of 9 March would be available at about 0200 UTC 10 March, and the 48-h forecast started at 1200 UTC 8 March would be available at about 0200 UTC of the day before (by contrast, the analysis for 1200 UTC 10 March would be available only at about 2300 UTC 10 March). Thus, by using the 24-h forecast started at 1200 UTC 9 March to define the initial conditions for our 48-h singular vector computation (to give the reader a reference value, in the current configuration less than 1 h is required to compute about 10 singular vectors at T63L19 resolution; note that this time can be easily reduced by using more computing processors) at about 0300 UTC 10 March, all the necessary information could be passed to the flight crew.

This example illustrates the reason why it is of interest to investigate the impact on the singular vectors of using different trajectories. Singular vectors have been computed following three different trajectories, one starting from the analysis of the day, one from the 24-h forecast of the day before, and one starting from the 48-h forecast of two days before (Table 2).

c. Naming convention

For each case study, singular vectors have been named according to the verification area and to the trajectory forecast time used to define the initial conditions for the singular vector computation, using letters A, B, and C to identify the area and using numbers 0, 1, and 2 to identify whether the analysis, the 1-day, or the 2-day forecast was used. Thus, 0-type singular vectors are singular vectors computed following a trajectory started from the analysis, and A-type singular vectors are singular vectors computed with the A verification area. For example, the C2 label identifies singular vectors computed to have maximum final time norm in the verification area C following the trajectory started from the 48-h forecast started two days before the target time.

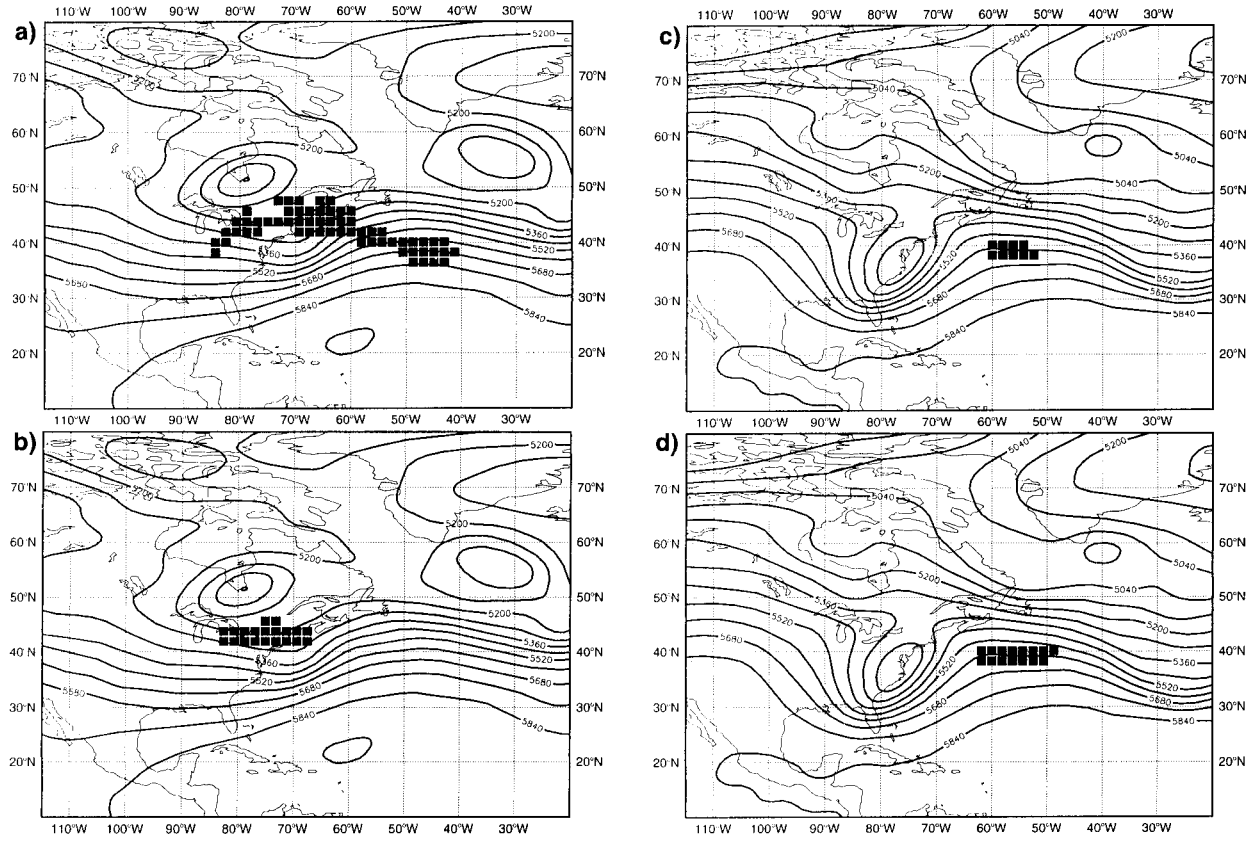

FIG. 4. The A0 target area defined using the first four singular vectors as the grid points $s \in \Sigma_0$ where $F_4^E(s) \geq 0.5F_4^E(s_0)$, with $F_4^E(s_0)$ being the maximum of the function F_4^E, and 500-hPa geopotential height at 1200 GMT for (a) 2 Jan, (c) 6 Jan, (e) 5 Feb, (g) 7 Feb, and (i) 10 Mar 1996; and the A1 target area defined using the first four singular vectors as the grid points where $F_4^E(s) \geq 0.5F_4^E(s_0)$, with $F_4^E(s_0)$ being the maximum of the function F_4^E, and 500-hPa geopotential height at 1200 UTC for (b) 2 Jan, (d) 6 Jan, (f) 5 Feb, (h) 7 Feb, and (j) 10 Mar 1996. Contour interval for geopotential height is 80 m.

d. Nonlinear integrations

Nonlinear integrations have been performed at the same resolution of singular vector computation (T63L19), and with the same version of the ECMWF model (cycle 18r3).

4. Synoptic description

A brief synoptic description of the five case studies is reported. All cases focus on system developments occurring during a 48-h time period starting at 1200 UTC. These five winter cases were chosen because they are characterized by cyclone developments in the Atlantic, and because the 48-h forecast error was larger than average.

a. The 2 January 1996 case study

On 2 January, a low with three surface centers (965–970 mb) extends between 80° and 20°W, at about 50°N. The system is characterized by a westward tilt with height. After 24 hours, a large depression dominates the Atlantic. On 4 January (Fig. 1a), the main circulation is dominated by a deep low located at about 55°N, 35°W. At the surface, a small-scale depression (995 mb) is located just southwest of Cornwall, east of a secondary low positioned at 50°N, 20°W (Fig. 1b).

b. The 6 January 1996 case study

On 6 January, a small surface low (990 mb) is located at 42°N, 50°W, while the east Atlantic is dominated by a large-scale depression with a double low pressure center. The system has vertical structure but not much tilt with height. After 24 hours the surface low pressure has deepened (965 mb), is located at 46°N, 32°W, and has started interacting with the other systems. This evolution can be defined as a case of explosive cyclogenesis, since the surface low deepened by more than 24 mb in a day. After 12 hours, it has developed, becoming the principal system in the eastern Atlantic. On 8 January, the low has further deepened (955 mb at surface), and is at 51°N, 21°W (Figs. 1c,d).

c. The 5 February 1996 case study

On 5 February, a very elongated cold front crosses the Atlantic from Central America to the United King-

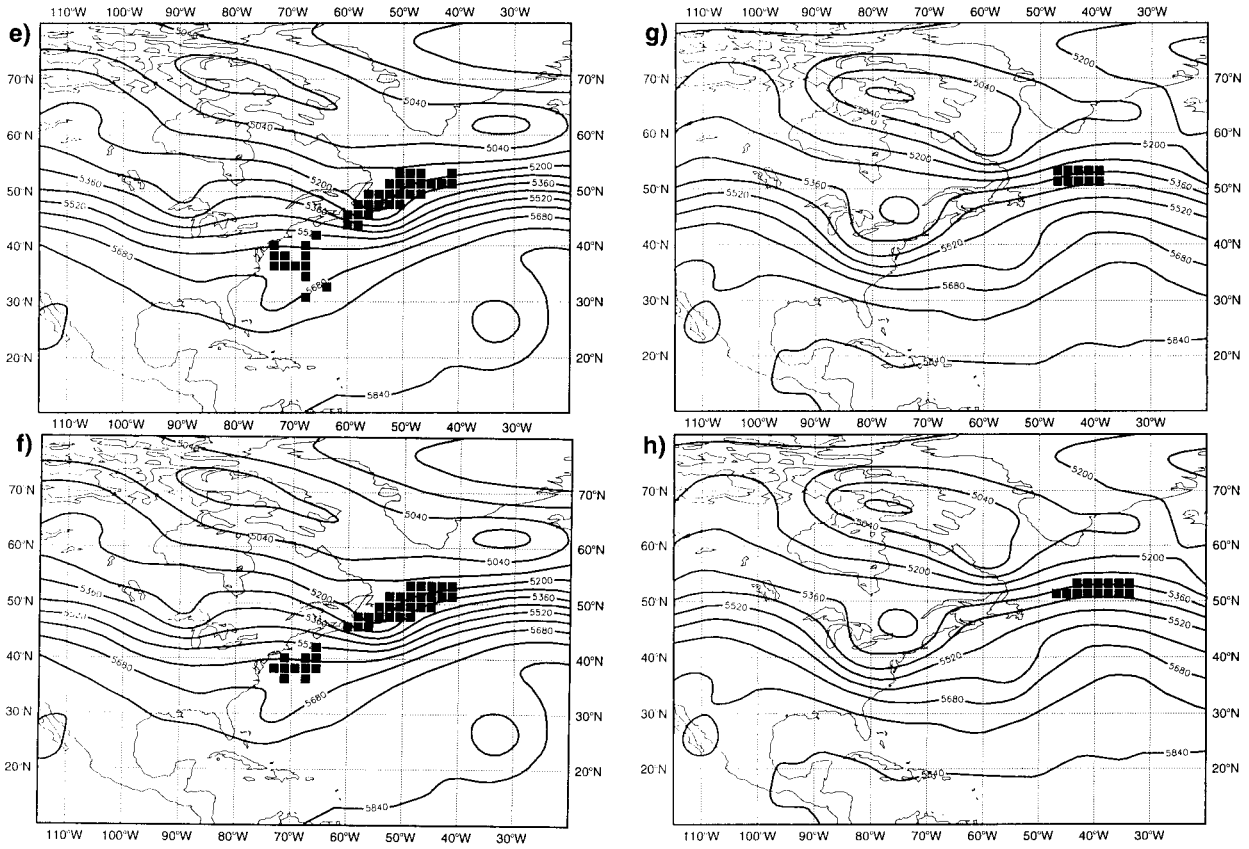

FIG. 4. (*Continued*)

dom, with a frontal surface low (995 mb) developing at about 48°N, 40°W. The system is characterized by a slight westward tilt with height. After 24 hours, the surface minimum (985 mb) is west of Ireland, and 12 hours later is between England and France. On 7 February, the system has moved to France (minimum of 980 mb) at about 47°N, 8°E (Figs. 1e,f).

d. The 7 February 1996 case study

On 7 February, an elongated front is positioned over the Atlantic, with a low (1010 mb) located at 42°N, 45°W. A marked westward vertical tilt characterizes the system. After 24 hours, the system has deepened (975 mb) and progressed to 52°N, 25°W. On 9 February, the low pressure system (965 mb) is positioned at 56°N, 12°W (Figs. 1g,h).

e. The 10 March 1996 case study

On 10 March, the so-called Icelandic low, with a minimum of 955 mb at 60°N, 35°W, is dominating the North Atlantic. The system is characterized by a westward tilt with height. A front originates in the low center and extends throughout the entire ocean, with kinks in surface pressure in the middle Atlantic. After 12 hours, the elongated front gives rise to a very small trough at 52°N, 16°W, and 24 hours later a warm front is just west of England and is crossing Scotland. On 12 March (Fig. 1i), a deep trough is evident in the midwestern Atlantic, and a secondary low pressure system (1010 mb) suddenly develops at 50°N, 10°W, on the preexisting elongated front (Fig. 1j).

5. Trajectory forecast error and sensitivity experiments

First, the accuracy of the trajectory forecast is investigated. Then, the singular vector sensitivity to the trajectory and the verification area is analyzed. Finally, the sensitivity of the target area to the trajectory, the verification area, and the number of singular vectors is discussed.

a. Trajectory forecast error

Forecasts of the 850-hPa vorticity field have been used to set the verification area Σ_t, which defines the local projection operator $\mathbf{T}$ used in the singular vector computation [see Eqs. (8)–(9)]. Thus, it is important to know the accuracy of 48-, 72-, and 96-h forecasts (ver-

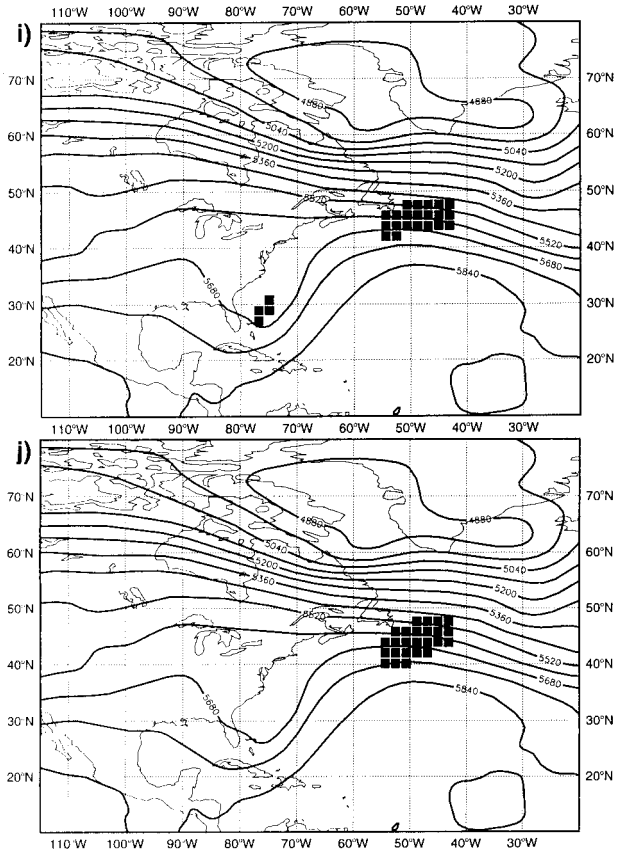

FIG. 4. (*Continued*)

ifying at the same time) in predicting 850-hPa vorticity maxima.

Considering the region around the British Isles, the poorest agreement between a 72-h forecast and the analysis is achieved for the 2 January case study (Figs. 2a,b), with the forecast missing the prediction of the analyzed vorticity maximum at about 50°N, −5°E. The vorticity maximum south of Cornwall is predicted but underestimated for the 5 February case (Figs. 2e,f), the vorticity maximum is misplaced in the 10 March case (Fig. 2i,j), while there is a rather good agreement between the general features in the forecast and analysis in the other two cases.

For all cases, a better agreement is shown between a 48-h forecast and the analysis. For the 2 January case study, for example, the 48-h forecast presents a vorticity structure more similar to the analysis, with maxima around 55°N, −5°E; 50°N, −20°E; and 60°N, −20°E (not shown). Instead of this, a rather poor agreement between the 96-h forecast and the analysis is shown in two out of five cases (specifically, for 2 January and for 5 February, not shown).

b. Singular vector sensitivity

A measure of the similarity between the two unstable subspaces defined by the first M singular vectors computed in any two configurations is given by the so-called similarity index (Buizza 1994a), which gives the average percentage of total energy of any singular vector in one set explained by the other set of singular vectors. The similarity index is 100% for two parallel unstable subspaces, and it is 0% for orthogonal subspaces. As a reference value, the similarity index between the unstable subspaces generated by the first 10 singular vectors of two consecutive days (i.e., computed with initial conditions differing by 2 days) is about 30% (Buizza 1994a, 1998).

Table 3a shows that the similarity index between the first 10 0- and 1-type singular vectors is the largest (about 60%). If unstable subspaces generated by the first four (instead of the first 10) singular vectors are considered, the average value of the similarity indexes is similar and the standard deviation is larger. By contrast, poor similarity is shown if one considers the leading singular vector only. Considering, for example, configurations A0 and A1, the mean and standard deviation of the similarity indices are $s_m = 43$ and $s_{\text{std}} = 29$ if one considers the leading singular vector only; $s_m = 62$ and $s_{\text{std}} = 16$ if one considers the first 4 singular vectors; and $s_m = 59$ and $s_{\text{std}} = 8$ (Table 3a) if one considers the first 10 singular vectors. Table 3a also indicates that 0- and 2-type singular vectors are less similar (similarity index about 36%).

Note that the similarity between 0- and 1-type singular vectors is higher than the similarity between 1- and 2-type singular vectors. This is because 1-type trajectories are closer to 0-type trajectories (i.e., analyses) than 2-type trajectories. (Considering the 500-hPa geopotential height field for the five cases discussed in this work, the average rms distance 0–1 is 16 m at initial time and 29 m at forecast day 2; the average rms distance 1–2 is 22 m at initial time and 32 m at forecast day 2; and the average rms distance 0–2 is 29 m at initial time and 41 m at forecast day 2.)

Two important conclusions can be drawn. First, using a forecast instead of the analysis as initial condition for singular vector computation can change the singular vector structure. This is particularly evident if a 2-day forecast is used as initial condition instead of the analysis. Second, the more singular vectors are used to define the unstable subspace, the smaller the impact of the trajectory on the unstable subspace definition.

For a given trajectory type, let us now examine the singular vector sensitivity to the verification area. Table 3b indicates that the initial time similarity indexes of unstable subspaces generated by the first 10 singular vectors computed with different verification areas are rather similar. Note that the comparison of Tables 3a and 3b shows that, within the limits of our trajectory and area variations, results are more sensitive to the trajectory definition than to the choice of the verification area. This lower sensitivity to the verification area is an important result, because it suggests that, if errors in the forecast trajectory are not too large, targeting is feasible.

c. Target area sensitivity

First, the sensitivity of the location s_0 where the grid-point total energy F_M^E is maximum [see Eqs. (10)–(11)] is analyzed.

Concerning the sensitivity to the number of singular vectors, results indicate that the maxima identified by using the first 4 or 10 singular vectors are very close (not shown). By contrast, these maxima differ from the ones identified by the leading singular vector only.

Regarding the impact of the trajectory definition, Fig. 3 shows that, for any verification area, 0- and 1-type maxima are located very close to each other, while 2-type maxima can be far from them. Quantitatively, Fig. 3 shows that maxima computed using 0- and 1-type trajectories differ on average by less than 10°, and that maxima computed using 0- and 2-type trajectories differ by more than 15° (note that a T63 spectral resolution corresponds in physical space to a grid interval of 1.8°). As it was the case for the singular vectors, results indicate a low sensitivity to the verification area. In fact, apart from the 2 January case, maxima computed with different verification areas but with the same trajectory differ on average by less than 5°. The complex synoptic situation of the 2 January case, with many interacting vortices (Fig. 2a), is certainly one of the causes for this (note that there is a unique dominant cyclone inside the verification region in the other cases; Figs. 2b–e).

Thus, these results indicate that initial conditions defined by forecasts older than 24 h should not be used, that more than 4 singular vectors should be used to reduce possible errors due to using a forecast instead of the analysis as initial condition, and that there are little differences between maxima identified using 4 or 10 singular vectors.

Consider how not only the maximum value of the total energy function F_M^E but the whole target areas computed using A0 or A1 singular vectors (Fig. 4). Generally speaking, results indicate that each target area is centered around the maximum of the function F_4^E with shape dependent on the case study. For three cases (6 January, and 5 and 7 February), the A0 and A1 target areas are very similar, while some differences appear for the other two cases (2 January and 10 March). For the 2 January case, the A1 target area (Fig. 4a) is more localized than the A0 one (Fig. 4b), and for the 10 March case the A0 target area presents a subregion at 30°N (Fig. 4i) that is absent in the A1 target (Fig. 4j). Note that, by definition, the target area depends on the choice of the 0.5 value in Eq. (12), and that lower (higher) values do restrict (enlarge) the target region, since the definition of the target area depends on the choice of the constant on the right-hand side of the inequality in Eq. (12). The reader is referred to section 7 for further discussion on Eq. (12), and more generally on the precise definition of the target area. Concerning the sensitivity of the entire target area to the singular vector number, target areas based on 10 and 4 singular vectors are very similar (not shown).

6. Estimation of possible forecast error reduction using pseudo-inverse initial perturbations

Following the results reported in section 5, only A0 and A1 singular vectors are considered hereafter. First, for each case study, the error of the forecast started from the analysis $\mathbf{a}(t_0)$ (control forecast) is projected onto the leading singular vectors, and the pseudo-inverse initial perturbation $\boldsymbol{\delta}\tilde{\mathbf{e}}(t_0)$ is computed [see Eq. (18)]. Then, nonlinear integrations started from the analysis $\mathbf{a}(t_0)$ and from the perturbed analysis $\mathbf{a}(t_0) - \boldsymbol{\delta}\tilde{\mathbf{e}}(t_0)$ are compared to estimate the possible forecast error reduction that can be achieved by adding extra observations in the target area.

a. Potential reduction of the forecast error total energy norm

Denote by $\mathbf{c}(t)$ the control forecast, by $\mathbf{a}(t)$ the verifying analysis, and by $\mathbf{p}^{\mp}(t)$ the perturbed forecast computed integrating the nonlinear model from the perturbed initial condition $\mathbf{a}(t_0) \mp \boldsymbol{\delta}\tilde{\mathbf{e}}(t_0)$. Let us remind the reader that $\boldsymbol{\delta}\mathbf{e}(t) = \mathbf{c}(t) - \mathbf{a}(t)$ is the error of the control forecast (Fig. 5a), and that $\mathbf{L}'$ represents the components of the tangent forward propagator not included in the linear version (see section 2a).

If the time evolution of the pseudo-inverse initial perturbations can be linearly approximated by $\tilde{\mathbf{L}}$, then $\mathbf{p}^{-}(t)$ and $\mathbf{c}(t) - \boldsymbol{\delta}\tilde{\mathbf{e}}(t)$ should coincide, and the norm of the perturbed forecast error can be estimated as

$$\|\mathbf{p}^{-}(t) - \boldsymbol{a}(t)\|_E \approx \|\mathbf{c}(t) - \boldsymbol{\delta}\tilde{\mathbf{e}}(t) - \mathbf{a}(t)\|_E = [\|\boldsymbol{\delta}\mathbf{e}(t)\|_E^2 - \|\boldsymbol{\delta}\tilde{\boldsymbol{e}}(t)\|_E^2]^{1/2}. \quad (19)$$

This is schematically illustrated in Fig. 5b. Table 4a lists the norm of the control error $\boldsymbol{\delta}\mathbf{e}(t)$ and of the projected control error $\boldsymbol{\delta}\tilde{\mathbf{e}}(t)$, and Table 4b lists the expected error of the perturbed forecasts estimated by applying Eq. (19) (note that, since singular vectors have been maximized inside verification area A, all norms in Table 4 have been computed inside this area). Tables 4a,b indicate that the forecast error structure is slightly better captured by the A0 than by the A1 singular vectors, and that the forecast error reduction almost doubles when using 4 instead of only the leading singular vector, while it increases only slightly when using 10 instead of 4 singular vectors. Table 4b shows that for pseudo-inverse perturbations constructed using the first four singular vectors, the norm of the perturbed forecast error is estimated to be between 3% and 15% smaller than the norm of the control forecast error.

This error reduction can be obtained only if the entire pseudo-inverse initial perturbation is used to perturb the analysis. In other words, if we consider the pseudo-inverse perturbation as an estimate of the initial analysis

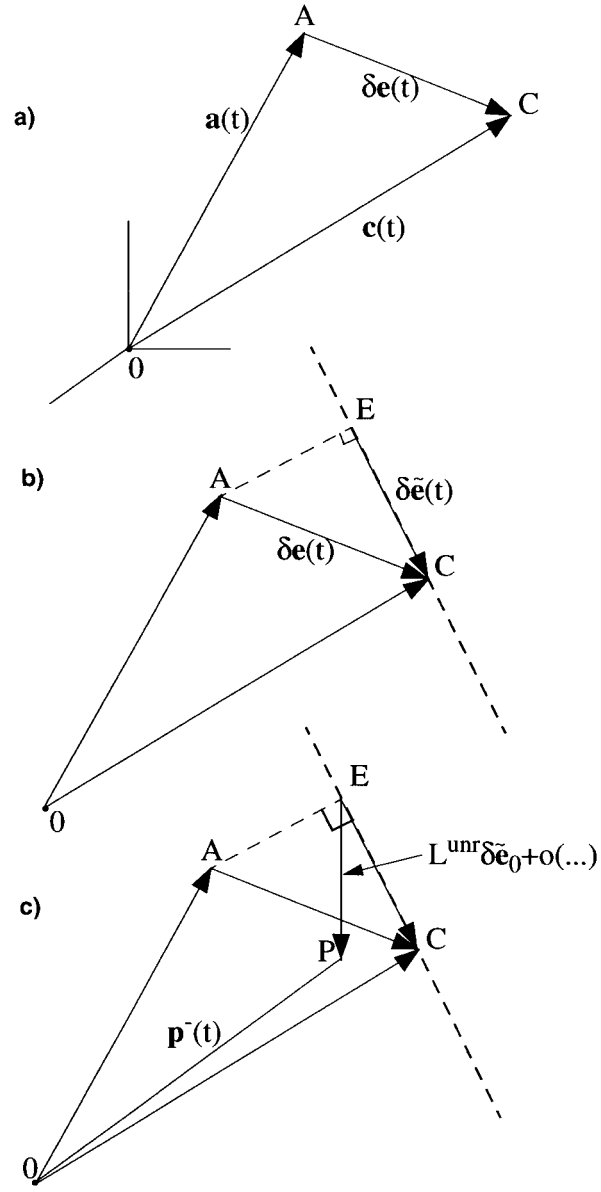

FIG. 5. Schematic of the contribution of the linear and nonlinear terms to the time evolution of the pseudo-inverse initial perturbations. (a) The forecast error $\boldsymbol{\delta}\mathbf{e}(t)$ (vector AC) is defined as the difference between the control forecast $\mathbf{c}(t)$ (vector OC) and the analysis $\mathbf{a}(t)$ (vector OA). (b) The projected forecast error $\boldsymbol{\delta}\tilde{\mathbf{e}}(t)$ (vector EC) is the projection of the forecast error $\boldsymbol{\delta}\mathbf{e}(t)$ on the leading four singular vectors: in the linear approximation, following Eq. (19), the perturbed forecast $\mathbf{p}^-(t)$ would be defined by vector OE. (c) Due to the contribution of the unresolved linear and nonlinear terms $-\mathbf{L}^{\text{var}}\boldsymbol{\delta}\tilde{\mathbf{e}}_0 + O(\|\boldsymbol{\delta}\tilde{\mathbf{e}}_0\|^2)$ (vector EP), the perturbed forecast $\mathbf{p}(t)$ is defined by vector OP.

error, a 15% forecast error reduction could be achieved only if the analysis error component associated with the leading singular vectors is eliminated in the whole area covered by the leading singular vectors. Since results showed little sensitivity to the number of singular vectors provided that the leading four were included, this estimate could be considered as an upper bound of the possible forecast error reduction.

TABLE 4a. Total energy norm ($m^2\ s^{-2}$) of the control forecast error $\boldsymbol{\delta}\tilde{\mathbf{e}}(t)$ and of the projected forecast error $\boldsymbol{\delta}\tilde{\mathbf{e}}(t)$ (inside the verification area A), with projections computed using the leading singular vector only, the first 4 or the first 10 singular vectors.

		$\|\boldsymbol{\delta}\tilde{\mathbf{e}}(t)\|_E$					
		SV 1		SV 1–4		SV 1–10	
Case study	$\|\boldsymbol{\delta}\mathbf{e}(t)\|_E$	A0	(A1)	A0	(A1)	A0	(A1)
96.01.02 → 04	146	33	(36)	59	(56)	61	(62)
96.01.06 → 08	126	5	(5)	32	(32)	40	(38)
96.02.05 → 07	143	16	(5)	59	(47)	66	(54)
96.02.07 → 09	170	50	(45)	57	(52)	62	(58)
96.03.10 → 12	192	89	(70)	101	(93)	110	(103)

Now, Table 4c lists the actual norm of perturbed forecasts, $\|\mathbf{p}^-(t) - \mathbf{a}(t)\|_E$. The comparison between Tables 4b and 4c shows that, generally speaking, this linear estimate is rather close to the 0%–13.5% error reduction in the perturbed nonlinear forecast for the four singular vector experiments, but there are also cases for which the error of the perturbed forecasts is far from the expected value from Eq. (19). Let us try to understand the reasons for this difference.

The perturbed forecasts $\mathbf{p}^{\mp}(t)$ started from the perturbed initial condition $\mathbf{a}(t_0) \mp \boldsymbol{\delta}\tilde{\mathbf{e}}(t_0)$ can be expressed in terms of the control forecast $\mathbf{c}(t)$ and of the pseudo-inverse initial perturbation in the following way:

$$\mathbf{p}^{\mp}(t) \approx \mathbf{c}(t) \mp (\mathbf{L} + \mathbf{L}')\boldsymbol{\delta}\tilde{\mathbf{e}}_0 + O(\|\boldsymbol{\delta}\tilde{\mathbf{e}}_0\|_E^2)$$

$$= \mathbf{c}(t) \mp [\tilde{\mathbf{L}} + (\mathbf{L} - \tilde{\mathbf{L}} + \mathbf{L}')]\boldsymbol{\delta}\tilde{\mathbf{e}}_0 + O(\|\boldsymbol{\delta}\tilde{\mathbf{e}}_0\|_E^2), \quad (20)$$

where $O(\|\boldsymbol{\delta}\tilde{\mathbf{e}}_0\|_E^2)$ denotes the quadratic term, $\boldsymbol{\delta}\tilde{\mathbf{e}}_0 = \boldsymbol{\delta}\tilde{\mathbf{e}}(t_0)$; and where higher-order terms have been neglected. Since the control forecast, the linear term $\tilde{\mathbf{L}}\boldsymbol{\delta}\tilde{\mathbf{e}}_0$, and both the positive and the negative perturbed forecasts are known, the magnitude of the other terms can be computed as follows:

$$\|O(\|\tilde{\mathbf{e}}_0\|_E^2)\|_E \approx \frac{1}{2}\|\mathbf{p}^- + \mathbf{p}^+ - 2\mathbf{c}\|_E, \quad (21a)$$

$$\|\mathbf{L}^{\text{unr}}\boldsymbol{\delta}\tilde{\mathbf{e}}_0 + O(\|\boldsymbol{\delta}\tilde{\mathbf{e}}_0\|_E^2)\|_E \approx \|\mathbf{p}^+ - \mathbf{c} - \mathbf{L}\boldsymbol{\delta}\tilde{\mathbf{e}}_0\|_E, \quad (21b)$$

where $\mathbf{L}^{\text{unr}} \equiv \mathbf{L} - \tilde{\mathbf{L}} + \mathbf{L}'$.

Table 4d lists the norm of the nonlinear terms. Com-

TABLE 4b. Expected norm of the error of the perturbed forecast estimated linearly using Eq. (19).

	$[\|\boldsymbol{\delta}\mathbf{e}(t)\|_E^2 - \|\boldsymbol{\delta}\tilde{\mathbf{e}}(t)\|_E^2]^{1/2}$					
	SV 1		SV 1–4		SV 1–10	
Case study	A0	(A1)	A0	(A1)	A0	(A1)
96.01.02 → 04	142	(141)	133	(134)	132	(132)
96.01.06 → 08	125	(125)	122	(122)	119	(120)
96.02.05 → 07	142	(143)	130	(135)	127	(132)
96.02.07 → 09	162	(164)	160	(162)	158	(160)
96.03.10 → 12	170	(178)	163	(168)	157	(162)

TABLE 4c. Norm of the perturbed forecast error.

	$\|\mathbf{p}^-(t) - \mathbf{a}(t)\|_E$					
	SV 1		SV 1–4		SV 1–10	
Case study	A0	(A1)	A0	(A1)	A0	(A1)
96.01.02 → 04	145	(146)	141	(143)	141	(142)
96.01.06 → 08	124	(125)	118	(121)	116	(116)
96.02.05 → 07	142	(143)	128	(137)	125	(136)
96.02.07 → 09	161	(162)	157	(160)	156	(161)
96.03.10 → 12	176	(192)	166	(183)	157	(179)

pared to the linear terms $\tilde{\mathbf{L}}\boldsymbol{\delta}\tilde{\mathbf{e}}_0$ (Table 4a), the quadratic terms are always smaller apart for the 6 January case with pseudo-inverse perturbations constructed using the leading singular vector only.

Table 4e lists the norm of the sums of the unresolved linear and the quadratic terms. Table 4e shows that these sums have the same magnitude of the linear terms $\tilde{\mathbf{L}}\boldsymbol{\delta}\tilde{\mathbf{e}}_0$ (Table 4a). This indicates that the differences between the expected error from Eq. (19) and the actual forecast error reduction is mainly due to the unresolved linear processes more than to nonlinear processes.

Figure 5c shows schematically how the sum of the linear term $-\boldsymbol{\delta}\tilde{\mathbf{e}}(t) = -\tilde{\mathbf{L}}\boldsymbol{\delta}\tilde{\mathbf{e}}_0$ and the unresolved linear and quadratic terms $-\mathbf{L}^{\text{unr}}\boldsymbol{\delta}\tilde{\mathbf{e}}_0 + O(\|\boldsymbol{\delta}\tilde{\mathbf{e}}_0\|_E^2)$ can keep the perturbed forecast $\mathbf{p}^-(t)$ closer than expected to the control forecast $\mathbf{c}(t)$. This is confirmed by Table 4f, which lists the norm of the distance $\mathbf{p}^-(t) - \mathbf{c}(t)$. As a consequence, the error of the perturbed forecast can remain very similar to the control error. This is further confirmed by the fact that the projection of the error of the perturbed forecasts $\mathbf{p}^{\mp}(t)$ onto the leading singular vectors is not null, and it has a magnitude comparable (although smaller) to the control error projection.

These results indicate that the current version of the linear model does not include linear contributions that are very important. As a consequence, although we found on average an agreement between the linear and the nonlinear estimates of the potential forecast error reduction, results indicate that a precise quantitative estimate of potential forecast error reduction cannot be achieved with the present system.

Care must be taken in generalizing these results to singular vectors computed with more physical processes, for example, to singular vectors computed with moist processes. In fact, the inclusion of moist processes in the tangent forward and adjoint models could change the structure of the singular vectors substantially. As a consequence, the relative importance of linear and nonlinear processes in the time evolution of singular vectors computed with moist processes can be different from the current one.

TABLE 4d. Norm of the nonlinear term.

	$\|O(\|\boldsymbol{\delta}\tilde{\mathbf{e}}_0\|_E^2)\|_E$					
	SV 1		SV 1–4		SV 1–10	
Case study	A0	(A1)	A0	(A1)	A0	(A1)
96.01.02 → 04	7	(8)	10	(8)	9	(8)
96.01.06 → 08	10	(9)	10	(9)	9	(7)
96.02.05 → 07	5	(5)	6	(9)	8	(7)
96.02.07 → 09	6	(8)	6	(7)	6	(6)
96.03.10 → 12	7	(6)	9	(7)	11	(10)

TABLE 4e. Norm of the sum of the unresolved linear and nonlinear terms.

	$\|\mathbf{L}^{\text{unr}}\boldsymbol{\delta}\tilde{\mathbf{e}}_0 + O(\|\boldsymbol{\delta}\tilde{\mathbf{e}}\|_E^2)\|_E$					
	SV 1		SV 1–4		SV 1–10	
Case study	A0	(A1)	A0	(A1)	A0	(A1)
96.01.02 → 04	30	(34)	59	(54)	60	(60)
96.01.06 → 08	13	(11)	31	(31)	40	(37)
96.02.05 → 07	14	(7)	59	(46)	65	(50)
96.02.07 → 09	50	(37)	58	(45)	62	(50)
96.03.10 → 12	88	(67)	91	(91)	95	(96)

b. *Synoptic evaluation*

For completeness, a synoptic view of the results discussed above is presented hereafter. Figure 6 shows, for each case study, the pseudo-inverse initial perturbations generated using the first four A0 singular vectors, in terms of vorticity and temperature at 850 hPa. The initial perturbations are very localized in space, with small horizontal and vertical scale, and with rather small initial amplitude. In fact, the contour interval for the pseudo-inverse vorticity is 100 times smaller than the contour interval used to plot the vorticity analysis in Fig. 2, and temperature local values are smaller than 1°.

Figures 7 and 8 show that the error of the control and the error of the perturbed forecast started adding the A0 initial perturbations for the two case studies with the larger forecast error reduction and with the higher sensitivity to the choice of the singular vector expansion basis (Table 4c). For the 5 February case study (Fig. 7), the control forecast error in verification area A is largest in the area near the deep surface low (Fig. 1f). Although there is an error reduction, only small differences between the control and perturbed forecast errors can be detected in the 850-hPa vorticity field (similar considerations can be drawn by considering the 500- and the 1000-hPa geopotential height, or 850-hPa temperature,

TABLE 4f. Norm of the difference between the perturbed and control forecasts.

	$\|\mathbf{p}^-(t) - \mathbf{c}(t)\|_E$					
	SV 1		SV 1–4		SV 1–10	
Case study	A0	(A1)	A0	(A1)	A0	(A1)
96.01.02 → 04	15	(14)	26	(20)	26	(19)
96.01.06 → 08	11	(12)	20	(14)	20	(17)
96.02.05 → 07	8	(6)	27	(29)	35	(26)
96.02.07 → 09	24	(16)	27	(19)	28	(20)
96.03.10 → 12	40	(24)	47	(34)	58	(41)

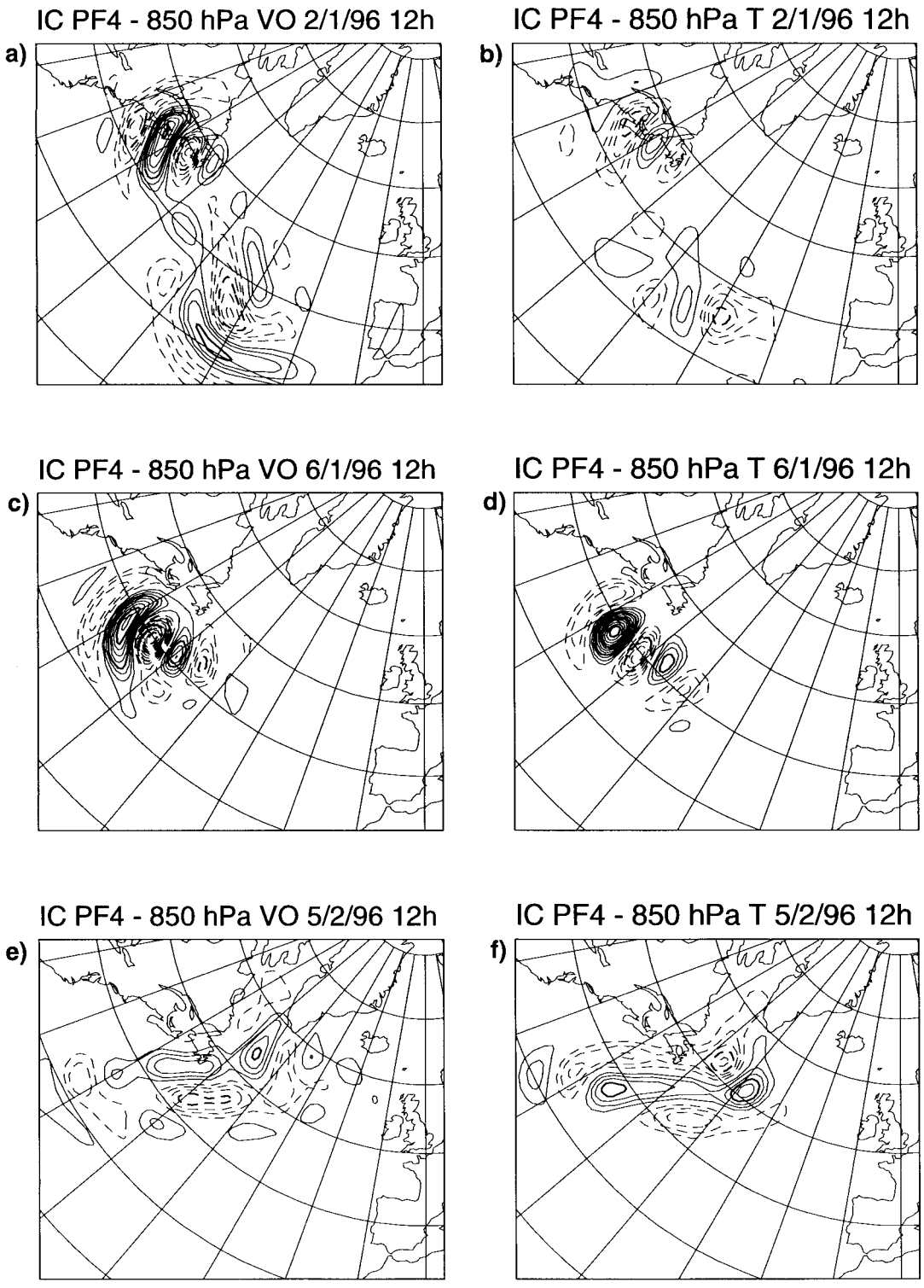

FIG. 6. The 850-hPa vorticity component of the pseudo-inverse initial perturbation generated using the first four A0 singular vectors for (a) 2 Jan, (c) 8 Feb, (e) 7 Feb, (g) 9 Feb, and (i) 12 Mar 1996; and the 850-hPa temperature component of the pseudo-inverse initial perturbation generated using the first four A0 singular vectors for (b) 2 Jan, (d) 8 Feb, (f) 7 Feb, (h) 9 Feb, and (j) 12 Mar 1996. Contour intervals are 0.03×10^{-5} s^{-1} (vorticity) and 0.05° (temperature).

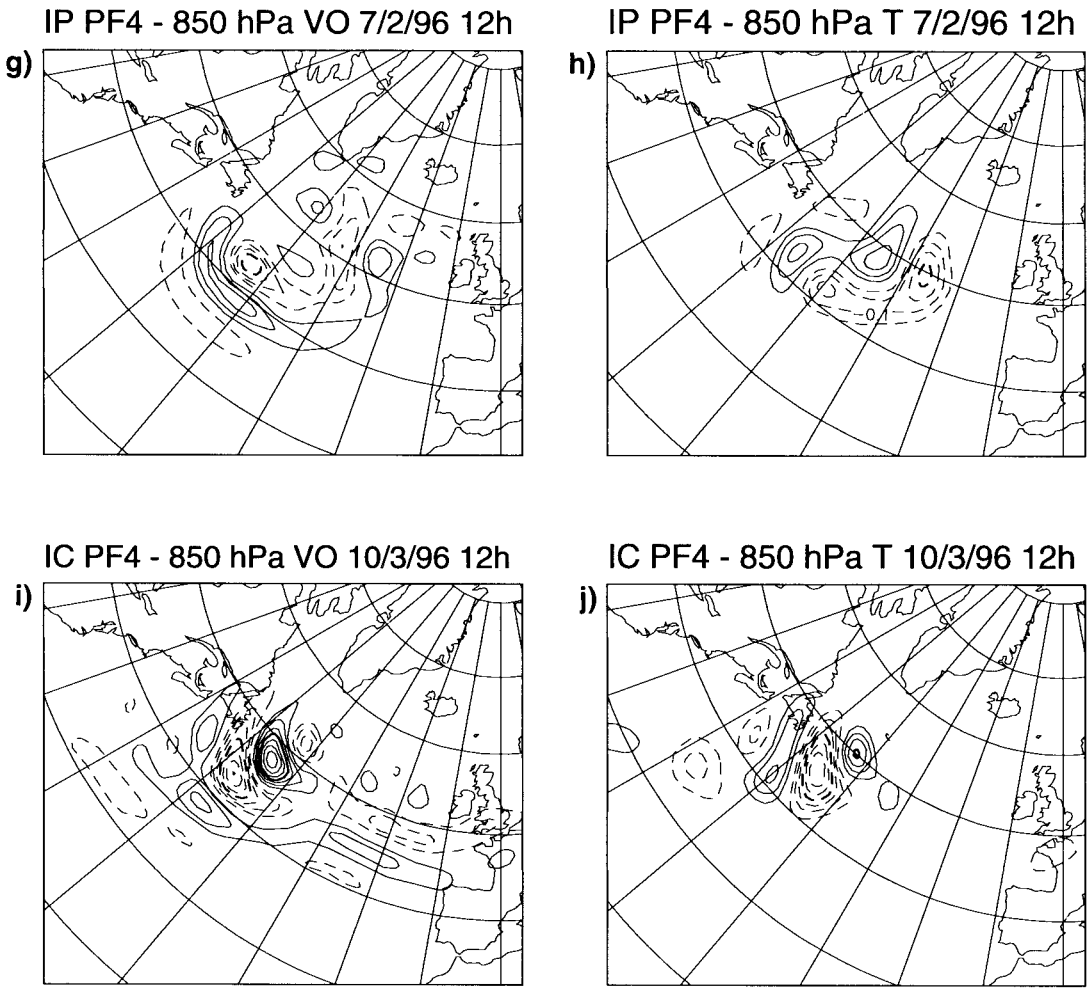

FIG. 6. (*Continued*)

not shown). For the 10 March case study (Fig. 8), slightly larger differences between the control and perturbed forecast errors can be seen.

Table 5 lists the root-mean-square error for geopotential height at 500 and 1000 hPa and for temperature at 850 hPa, of the control and perturbed forecasts with initial conditions perturbed with the A0 perturbations inside verification area A. Root-mean-square values for the four singular vector experiments confirm the result based on total energy norm that targeting adaptive observations can lead to about 13% error reduction.

7. Sensitivity of forecast error reduction to target area

One of the problems of real-time targeting is that extra observations can in some cases be taken only in a small region, and this can lead to only part of the target area Σ_0 being scanned. This is equivalent to being able to define the pseudo-inverse initial perturbation only in a restricted sector.

Let us focus on the results obtained using the first four singular vectors for 10 March. This case has been chosen because it is characterized by the largest forecast error reduction by means of the A0 pseudo-inverse initial perturbation (Table 4c). Furthermore, the A0 target area for this case consists of two rather distant target regions (Fig. 4i), and the vertical structure of the pseudo-inverse initial perturbation (Fig. 9) has a very strong vertical tilt with maximum values in correspondence of the two target regions, around $-45°$E in the lower troposphere and around $-70°$E at around 400 hPa (i.e., around model level 10).

To assess the impact on the forecast error of perturbing the control analysis with only part of the pseudo-inverse initial perturbation, 14 nonlinear integrations have been run, each of them with the analysis perturbed only by the pseudo-inverse initial perturbation (generated using the first four singular vectors) confined inside a specific square area. Experiments 1–10 are characterized by 20° areas, and experiments 11–14 by 40° areas.

Figure 10 shows, at the northwest corner of each ex-

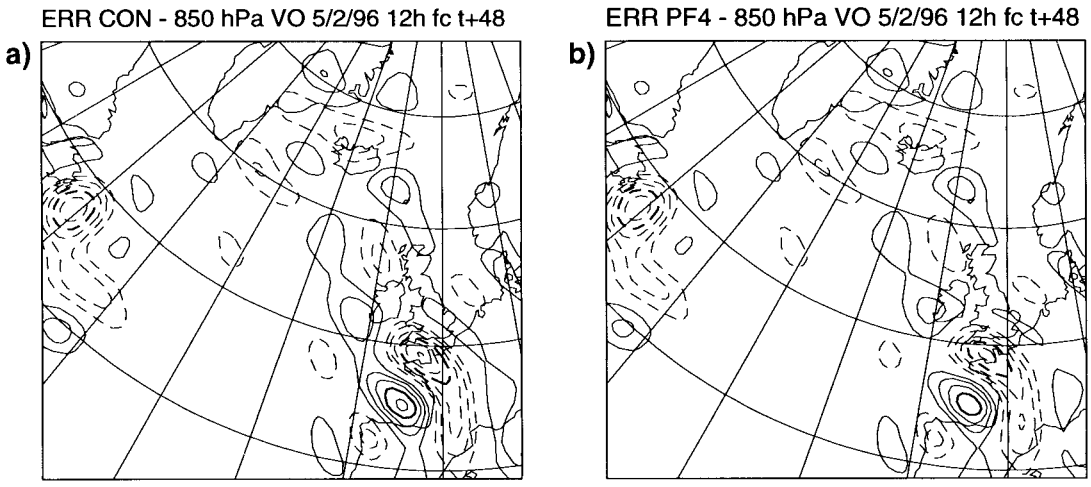

FIG. 7. The 850-hPa vorticity error of (a) the 48-h control forecast and (b) the 48-h perturbed forecast generated by adding the pseudo-inverse initial perturbations generated using the first four A0 singular vectors, for the 5 Feb case study. Contour interval is 3×10^{-8} s^{-1}.

periment area, the experiment number, the total energy norm of the perturbed forecast error started from the analysis perturbed by adding only the pseudo-inverse component inside the experiment area, and the dimension of the experiment area.

Generally speaking, Fig. 10 shows that restricting the pseudo-inverse initial perturbation moderates the forecast error reduction to values smaller than the one achieved by the perturbed forecast started by adding the entire A0 pseudo-inverse initial perturbation (166 m^2 s^{-2}). Area 3 (33°–13°N, 76°–56°W) is the 20° area characterized by the largest forecast error reduction (182 m^2 s^{-2}, compared to the 192 m^2 s^{-2} for the control error; see Table 4c). Note that this area is not located in correspondence of the peak of the gridpoint function F_4^E, but it is located around the southern of the two maxima in Fig. 4i, in correspondence to the high-level maximum of Fig. 9. A slightly larger error reduction characterizes the 40° area 13 (63°–23°N, 106°–66°W), with a perturbed forecast error norm of 175 m^2 s^{-2}. Note that area 13 includes the entire high-level maximum of Fig. 9.

These results indicate that care must be exerted when applying Eq. (12) to define the target area. On the one hand, the fact that extra observations can be taken only inside a small area suggests to set the constant at the right-hand-side of the inequality in Eq. (12) to a large value. On the other hand, to avoid the risk of not identifying sensitive regions this constant should not be set to values that are too large. The results reported in this paper suggest that a value of 0.5 is a reasonable choice.

8. Conclusions

Singular vectors identify perturbations with maximum growth during a finite time interval. Recent studies

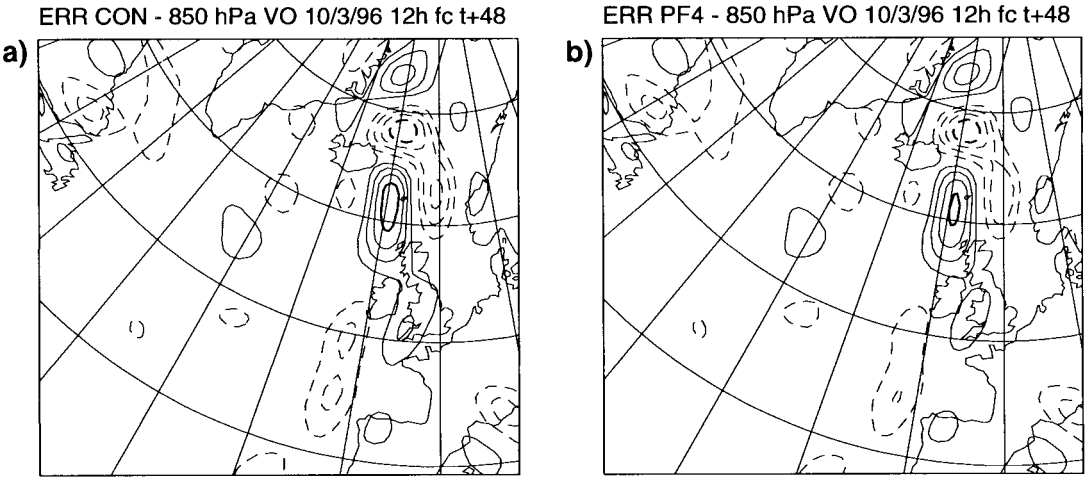

FIG. 8. As in Fig. 7 but for 10 Mar.

TABLE 5a. Root-mean-square error (inside the verification area A) of the control and the perturbed forecast started from initial conditions generated using A0 singular vectors for 500-hPa geopotential height (m).

Case study	Rmse control	Rmse control–pseudo		
		SV 1	SV 1–4	SV 1–10
96.01.02 → 04	28.7	26.9	26.4	26.7
96.01.06 → 08	19.6	19.9	19.8	19.5
96.02.05 → 07	32.6	32.2	30.1	30.1
96.02.07 → 09	26.2	23.0	22.7	22.6
96.03.10 → 12	57.2	53.2	52.6	49.9

TABLE 5b. Same as in Table 5a but for 1000-hPa geopotential height (m).

Case study	Rmse control	Rmse control–pseudo		
		SV 1	SV 1–4	SV 1–10
96.01.02 → 04	37.3	36.1	34.8	34.5
96.01.06 → 08	21.4	22.1	22.6	23.0
96.02.05 → 07	33.9	33.8	31.3	30.4
96.02.07 → 09	51.1	43.6	44.3	43.5
96.03.10 → 12	63.9	62.4	59.8	56.6

(Buizza et al. 1997; Gelaro et al. 1998) have demonstrated that they can capture fast growing features of forecast errors, and that pseudo-inverse perturbations constructed using singular vectors can provide an estimate of analysis errors.

The problem of targeting adaptive observations inside a target region Σ_0 to reduce the 48-h forecast error inside a verification area Σ_t, (Joly et al. 1996; Langland and Rohaly 1996; Snyder 1996; Bishop and Toth, 1998; Lorenz and Emanuel 1998; Palmer et al. 1998) has been discussed. A methodology based on singular vectors with maximum total energy norm inside the verification area Σ_t has been proposed. The target area Σ_0 has been identified by the grid points where a weighted sum of the total energy of the leading singular vector exceeds 0.5, its maximum value.

First, the sensitivity of the proposed methodology to the choice of the trajectory along which the singular vectors are evolved, to the choice of the final time verification area, and to the number of singular vectors used to identify the target area have been studied. Three different types of trajectories have been considered, defined as the forecasts started either from the analysis (0-type experiments), or from the 24- or 48-h forecasts started 1 or 2 days before the target time (respectively, 1- and 2-type experiments). Since the methodology has been applied to cyclone developments ending, at verification time, around the British Isles, three verification regions covering this region have been considered (Table 1). Computer power availability has limited the number of available singular vectors to 10 at most.

Results have shown that, within the limit of our choices, both singular vectors and the target area are little sensitive to the choice of the verification area. Considering 0- or 1-type trajectories, A, B, and C maxima of the function used to define the target area have been shown to differ by less than 5°. In contrast, results indicate a higher sensitivity to the trajectory definition, with maxima computed using 0- and 1-type trajectories on average differing by less than 10°, but with maxima computed using 0- and 2-type trajectories differing by more than 15°. This indicates that targeting should not be based on initial conditions defined by forecasts older than 24 h.

Results have also indicated that if more than four singular vectors are used, the impact of the trajectory is reduced, and the target area defined using singular vectors evolving along a trajectory started from the analysis or started from the 24-h forecast started one day before are very close. Concerning the number of singular vectors, small differences have been detected between targets defined using either 4 or 10 singular vectors.

Thus, our sensitivity analysis suggests that real-time targeting is feasible, despite operational constraints as the fact that only a forecast state can be used to start a singular vector computation, or that the verification region can be defined only approximately, or that the number of singular vectors that could be computed is limited.

The second part of this work focused on the problem of estimating the possible impact of targeted extra observations on the forecast error. Such an estimate has been computed by comparing nonlinear integrations started from the analysis (control forecast) with nonlinear integrations started from the analysis perturbed using so-called pseudo-inverse initial perturbations generated using the leading four singular vectors. Diagnostics based on either total energy norm or root-mean-square distance as a measure of forecast error have suggested that, on average, about 13% forecast error reduction could be achieved. It has to be stressed that this value has been estimated in the hypothesis that the analysis error component associated with the leading singular vectors is eliminated in the whole area covered by the leading singular vectors themselves. Results again indicated a low sensitivity to the number of singular vectors beyond including the four leading ones, confirming the dominant role of the leading singular vectors documented by Gelaro et al. (1998). It should also be stressed that this estimate of 13% error reduction is based on five specially selected cases of cyclone de-

TABLE 5c. Same as in Table 5a but for 850-hPa temperature (degrees).

Case study	Rmse control	Rmse control–pseudo		
		SV 1	SV 1–4	SV 1–10
96.01.02 → 04	1.5	1.4	1.3	1.3
96.01.06 → 08	1.4	1.4	1.4	1.4
96.02.05 → 07	1.8	1.8	1.7	1.7
96.02.07 → 09	1.9	1.7	1.7	1.7
96.03.10 → 12	1.7	1.6	1.5	1.4

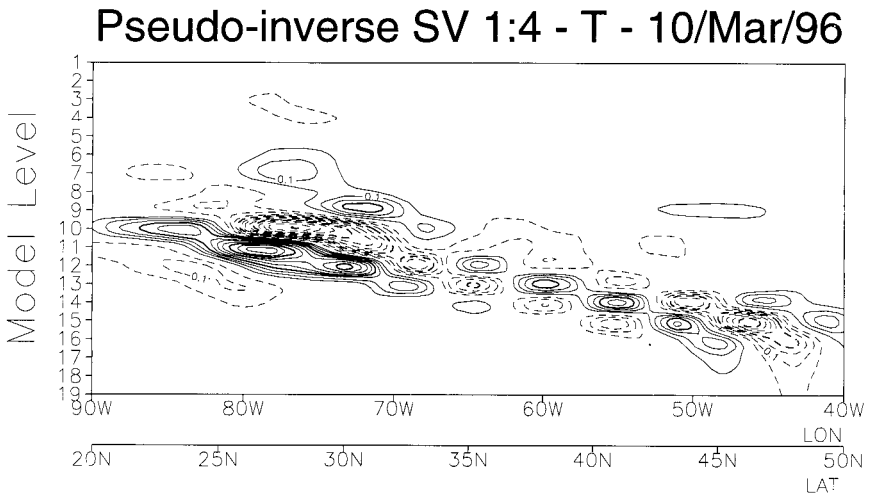

FIG. 9. Vertical cross section of the temperature component of the pseudo-inverse initial perturbation constructed using the first four singular vectors, from 25°N (100°W) to 50°N (20°W). Contour interval is 0.05°.

velopment in the Atlantic Ocean, and thus can be overly optimistic.

Results have also indicated that this estimate, based on the comparison of nonlinear integrations, can be far from the linear estimate given by the projection of the control forecast error onto the evolved singular vectors. The main reason for this discrepancy appears to be the fact that the linear and adjoint model versions used in this study include only a few components of the tangent version of the nonlinear model. This supports the need for including other physical processes (moist processes, radiation, gravity wave drag, convection; see Errico and Ehrendorfer 1995; Buizza et al. 1996) in the linear and adjoint model versions to decrease the inconsistency between linear and nonlinear integrations.

Finally, the impact of restricting the initial time pseudo-inverse perturbations to subregions of the target area has been investigated. Results have indicated that such a restriction can limit the error reduction to about 65% of the full potential value. This result should be taken into account in future studies of real-time targeting, which for practical and technical reasons are usually based on extra observations that sample only small regions.

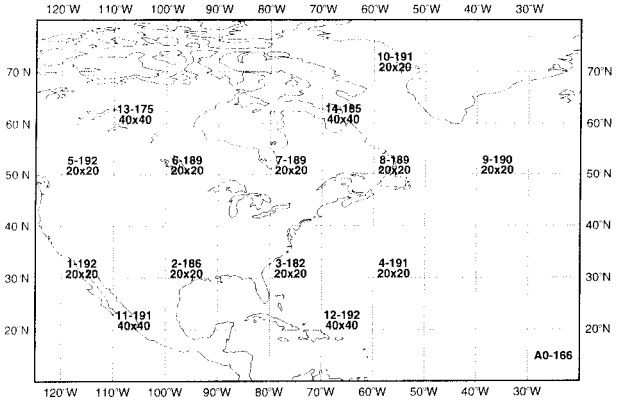

FIG. 10. The 10 Mar case study. For the 14 sensitivity experiments (see text), the experiment number, the total energy norm of the perturbed forecast error, and the dimension of the area (where the pseudo-inverse component has been used) are reported at the northwest corner of the area itself.

Acknowledgments. We thank Prof. A. J. Thorpe and Dr. T. N. Palmer for their valuable suggestions and guidance given during the development of this work. We are also thankful to Ron Gelaro for his highlighting comments to an earlier version of this manuscript, and to Craig Bishop, Chris Snyder, and Zoltan Toth for their very careful revision of the manuscript.

REFERENCES

Appenzeller, Ch., H. C. Davies, J. M. Popovic, S. Nickovic, and M. B. Gavrilov, 1996: PV morphology of a frontal-wave development. *Meteor. Atmos. Phys.,* **58,** 21–40.

Barkmeijer, J., M. van Gijzen, and F. Bouttier, 1998: Singular vectors and estimates of the analysis error covariance metric. *Quart. J. Roy. Meteor. Soc.,* **124,** 1695–1713.

Bishop, C. H., and Z. Toth, 1998: Ensemble transformation and adaptive observations. *J. Atmos. Sci.,* **56,** 1748–1765.

Borges, M., and D. L. Hartmann, 1992: Barotropic instability and optimal perturbations of observed nonzonal flows. *J. Atmos. Sci.,* **49,** 335–354.

Buizza, R., 1994a: Sensitivity of optimal unstable structures. *Quart. J. Roy. Meteor. Soc.,* **120,** 429–451.

——, 1994b: Localization of optimal perturbations using a projection operator. *Quart. J. Roy. Meteor. Soc.,* **120,** 1647–1682.

——, 1998: Impact of horizontal diffusion on T21, T42, and T63 singular vectors. *J. Atmos. Sci.,* **55,** 1069–1083.

——, and T. N. Palmer, 1995: The singular-vector structure of the atmospheric general circulation. *J. Atmos. Sci.,* **52,** 1434–1456.

——, J. Barkmeijer, R. Gelaro, and J.- F. Mahfouf, 1996: Singular vectors, norms and large-scale condensation. Preprints, *11th Conf. on Numerical Weather Prediction,* Norfolk, VA, Amer. Meteor. Soc., 50–51.

——, R. Gelaro, F. Molteni, and T. N. Palmer, 1997: The impact of increased resolution on predictability studies with singular vectors. *Quart. J. Roy. Meteor. Soc.,* **123,** 1007–1033.

Courtier, P., and Coauthors, 1993: Variational Assimilation at ECMWF. ECMWF Research Department Tech. Memo. 194, 84 pp. [Available from ECMWF, Shinfield Park, Reading, Berkshire RG2 9AX, United Kingdom.]

Errico, E. R., and M. Ehrendorfer, 1995: Moist singular vectors in a primitive-equation regional model. Preprints, *10th Conf. on Atmospheric and Oceanic Waves and Stability,* Big Sky, MT, Amer. Meteor. Soc., 235–238.

Farrell, B. F., 1990: Small error dynamics and the predictability of atmospheric flows. *J. Atmos. Sci.,* **47,** 2409–2416.

Gelaro, R., R. Buizza, T. N. Palmer, and E. Klinker, 1998: Sensitivity analysis of forecast errors and the construction of optimal perturbations using singular vectors. *J. Atmos. Sci.,* **55,** 1012–1037.

Hoskins, B. J., M. E. McIntyre, and A. W. Robertson, 1985: On the use and significance of isentropic potential vorticity maps. *Quart. J. Roy. Meteor. Soc.,* **111,** 877–946.

Houtekamer, P. L., L. Lefaivre, J. Derome, H. Ritchie, and H. Mitchell, 1996: A system simulation approach to ensemble prediction. *Mon. Wea. Rev.,* **124,** 1225–1242.

Joly, A., and Coauthors, 1996: The Fronts and Atlantic Storm-Track Experiment (FASTEX): Scientific objectives and experimental design. *Bull. Amer. Meteor. Soc.,* **78,** 1917–1940.

Lacarra, J.-F., and O. Talagrand, 1988: Short range evolution of small perturbations in a barotropic model. *Tellus,* **40A,** 81–95.

Langland, R. H., and G. D. Rohaly, 1996: Adjoint-based targeting of observations for FASTEX cyclones. Preprints, *Seventh Conf. on Mesoscale Processes,* Reading, United Kingdom, Amer. Meteor. Soc., 369–371.

Lorenz, E., and K. A. Emanuel, 1998: Optimal sites for supplementary observations: Simulation with a small model. *J. Atmos. Sci.,* **55,** 399–414.

Molteni, F., R. Buizza, T. N. Palmer, and T. Petroliagis, 1996: The new ECMWF ensemble prediction system: Methodology and validation. *Quart. J. Roy. Meteor. Soc.,* **122,** 73–119.

Montani, A., R. Buizza, and A. J. Thorpe, 1996: Singular vector calculation for cases of cyclogenesis in the north Atlantic storm-track. Preprints, *Seventh Conf. on Mesoscale Processes,* Reading, United Kingdom, Amer. Meteor. Soc., 391–392.

Noble, B., and J. W. Daniel, 1977: *Applied Linear Algebra.* Prenctice-Hall, 477 pp.

Palmer, T. N., R. Gelaro, J. Barkmeijer, and R. Buizza, 1998: Singular vectors, metrics, and adaptive observations. *J. Atmos. Sci.,* **55.,** 633–653.

Pu, Z.-X., E. Kalnay, J. Sela, and I. Szunyogh, 1997: Sensitivity of forecast error to initial conditions with a quasi-inverse linear method. *Mon. Wea. Rev.,* **125,** 2479–2503.

——, ——, and Z. Toth, 1998: Application of the quasi-inverse linear and adjoint NCEP Global models to targeted observations during FASTEX. Preprints, *12th Conf. on Numerical Weather Prediction,* Phoenix, AZ, Amer. Meteor. Soc., 8–9.

Rabier, F., E. Klinker, P. Courtier, and A. Hollingsworth, 1996: Sensitivity of forecast errors to initial conditions. *Quart. J. Roy. Meteor. Soc.,* **122,** 121–150.

Snyder, C., 1996: Summary of an informal workshop on adaptive observations and FASTEX. *Bull. Amer. Meteor. Soc.,* **77,** 953–961.

Toth, Z., and E. Kalnay, 1993: Ensemble forecasting at NMC: The generation of perturbations. *Bull. Amer. Meteor. Soc.,* **74,** 2317–2330.

——, and ——, 1996: Ensemble forecasting at NCEP. *Proc. European Centre for Medium-Range Weather Forecasts Sem. on Predictability,* Vol. II, Reading, United Kingdom, ECMWF, 39–61.